Key Engineering Materials Vols. 342-343 (2007) pp. 465-468
online at http://www.scientific.net

Preparation of Naphthalocyanine Dendrimer Loaded Polyion Complex Micelle for Photodynamic Therapy

Woo-Dong Jang[1], Nobuhiro Nishiyama[2,5] and Kazunori Kataoka[2,3,4,5]

[1] Department of Chemistry, College of Science, Yonsei University, 134 Sinchondong, Seodaemun-gu, Seoul 120-749, Korea

[2] Center for Disease Biology and Integrative Medicine, The University of Tokyo, 7-3-1 Hongo, Bunkyo-ku, Tokyo, 113-8656, Japan

[3]Department of Materials Engineering, Graduate School of Engineering, The University of Tokyo, 7-3-1 Hongo, Bunkyo-ku, Tokyo 113-8656, Japan

[4]Core Research for Evolutional Science and Technology (CREST), Japan Science and Technology Agency (JST)

[5]Center for NanoBio Integration, The University of Tokyo, 7-3-1 Hongo, Bunkyo-ku, Tokyo, 113-8656, Japan

wdjang@yonsei.ac.kr

Keywords: Dendrimer, Photosensitizer, Naphthalocyanine, Photodynamic therapy, Micelle

Abstract. A naphthalocyanine dendrimer (DNPcZn) was synthesized as a potential candidate of photosensitizer for photodynamic therapy. DNPcZn exhibited strong Q band absorption around 780 nm, a useful wavelength for high tissue penetration. A polyion complex (PIC) micelle (DNPcZn/m) system was formed via an electrostatic interaction of anionic DNPcZn and poly(ethylene glycol)-poly(L-lysine) block copolymers (PEG-b-PLL).

Introduction

Photodynamic therapy is based on the accumulation of a photosensitizer in malignant tissue. Subsequent illumination with laser light of an appropriate wavelength generates reactive oxygen species (ROS) which results in tissue destruction [1]. For an effective photodynamic effect, photosensitizers should be pure and have a high quantum yield of singlet oxygen generation. To obtain high quantum yields and effective energy absorption, photosensitizers must generally have large π-conjugation domains. Therefore, most of photosensitizers easily form aggregates, which provide a self-quenching effect of the excited state in aqueous medium due to their π-π interaction and hydrophobic characteristics. To overcome these problems, the structure of ionic dendrimer porphyrin is promising, because the substitution of large dendritic wedges

sufficiently prevents the formation of aggregates and provides high solubility in the aqueous medium. Furthermore, a charged ion surface can form polyion complex micelles by means of electrostatic interaction with an oppositely charged block copolymer. These types of polyion complex micelles with a PEG shell were demonstrated to accumulate effectively and specifically in solid tumor tissue due to the hyperpermeability of tumor capillaries. However, the dendrimer porphyrin has a relatively short wavelength absorption, where the absorption maximum is 430 nm, which is a limitation to improvement for practical PDT application [2,3]. In relation to this fact, several phthalocyanine molecules, including the one with a dendritic architecture, are of interest as a potential photosensitizer with appropriate wavelength absorption for practical PDT application. Herein, we report the first example of dendritic naphthalocyanine-incorporated polyion complex micelle formation.

Materials & Methods

Synthesis of block copolymer. PEG-*b*-PLL was synthesized by a previously reported procedure. Briefly, the *N*-carboxy anhydride of $N^{\square}$-Z-L-lysine was polymerized by initiation with CH_3O-PEG-NH_2 (12000 g/mol) in DMF under Ar, followed by deprotection of the Z group. GPC measurement of PEG-*b*-PLL exhibited single sharp peak at Mw of 16,600 and Mn of 16,300 based on PEG standards [4]. From the ^{1}H NMR measurement in D_2O, the polymerization degree of the PLL segment was determined to be 39.

Synthesis of dendrimer naphthalocyanine. Zinc naphthalocyanine (DNPcZn) was prepared from dimethyl-5-hydroxyisophthalate and 4-nitronaphthalonitrile. Briefly, the alkali mediated coupling reaction of G2 dendron (**1**), which was prepared from dimethyl-5-hydroxyisophthalate according to previous report, with 6-nitro-2,3-naphthalonitrile gave naphthalonitrile-cored G2 dendron (**2**). A mixture of **2** and $Zn(OAc)_2$ in *n*-hexanol was heated at 90 °C, and then a few drops of 1,8-diazabicyclo[5,4,0]undec-7-ene (DBU) were added. The mixture was refluxed with stirring overnight. The reaction mixture was chromatographed with silica gel to obtain dendrimer naphthalocyanine (DNPcZn). The DNPcZn was hydrolyzed using by 1 N NaOH solution to obtain ionic DNPcZn. **2**: yield 45%, ^{1}H NMR δ 8.24 (s, 4H, Ar-*H* in outer C_6H_3), 7.99-7.82 (m, 3H, Ar-*H* in naphthalonitrile), 7.76 (s, 8H, Ar-*H* in outer C_6H_3), 7.58-7.41 (m, 2H, Ar-*H* in nathalonitrile), 7.26 (s, 1H, Ar-*H* in inner C_6H_3), 7.17 (s, 2H, Ar-*H* in inner C_6H_3), 7.11 (s, 2H, Ar-*H* in mid C_6H_3), 7.04 (s, 4H, Ar-*H* in mid C_6H_3), 5.14 (s, 4H, outer -CH_2-), 5.10 (s, 8H, inner -CH_2-) 3.90 (s, 24H, -CH_3), **DNPcZn**: yield 26%, ^{1}H NMR δ 8.5-7.0 (br, 104H, Ar-*H*), 5.2 (br, 56H, -ArOCH_2-), 4.5 (br, 64H, -CO_2CH_2-), 1.7-1.1 (m, 256H, -CH_2-), 0.9-0.7 (m, 96H, -CH_3), MALDI-TOF-MS for $C_{463}H_{566}N_8O_{92}Zn$ *m/z*: calcd: 7780 [M^+]; found 7779.

Preparation of polyion complex micelle. Polyion complex micelles were made from ionic DNPcZn with PEG-b-PLL. In a typical procedure, the PEG-b-PLL was dissolved in an aqueous NaH_2PO_4 solution and added to an aqueous solution of DNPcZn in Na_2HPO_4 to give a solution containing polyion complex micelles. The ratio of positive charge to negative charge was fixed at 1:1 [5].

Measurements. The DLS measurements were performed using a Photal dynamic laser scattering DLS-7000 spectrometer (Otsuka Electronics Co., Ltd., Osaka, Japan) equipped with GLG3050 488 nm Ar laser (NEC Co., Ltd., Japan) and/or Zetasizer Nano ZS-90 (Malvern Co., Ltd., USA) with 532 nm laser irradiation. The UV-Vis and fluorescence spectra were measured using a V-550 spectrophotometer (JASCO, Tokyo, Japan) and Type 850 spectrofluorometer (Hitachi, Tokyo, Japan), respectively.

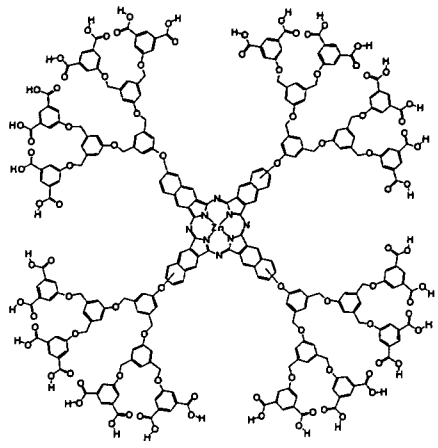

Figure 1. Dendrimer naphthalocyanine.

Results & Discussion

The synthesis of DNPcZn was accomplished by the method of Ng's group. Each step of synthesis was characterized by MALDI-TOF-MS and ^1H NMR measurement. The DNPcZn thus obtained was treated with a THF/H_2O mixture solution of NaOH to obtain ionic DNPcZn. DNPcZn exhibited significantly high solubility at various pH of the aqueous medium (over pH 4.3). Polyion complex micelle was prepared from negatively charged DNPcZn with oppositely charged PEG-*b*-PLL. In a typical procedure, the PEG-*b*-PLL (14.2 mg) was dissolved in an aqueous NaH_2PO_4 (10 mM, 6.15 mL) and added to a solution of DNPcZn (5 mg) in aqueous Na_2HPO_4 (10 mM, 13.85 mL) to give a solution containing polyion complex micelles encapsulating ionic DNPcZn (DNPcZn/m). The ratio of positive charge to negative charge was fixed at 1:1. After mixing the two solutions, the pH of the solution becomes 7.3 (10 mM PBS). The resulting micelle has a diameter of ca. 80 nm with a narrow size distribution (unimodal, $\mu 2/\Gamma^2 = 0.16$), determined by a dynamic light scattering measurement (DLS-7000 spectrometer; Otsuka Electronics Co., Ltd.).

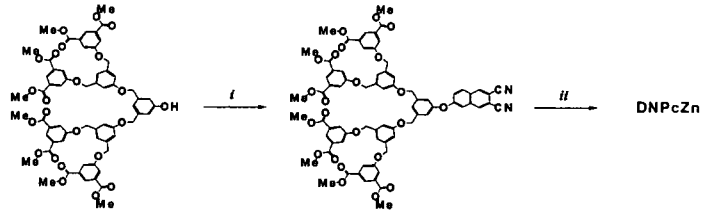

Figure 2. Synthesis of dendrimer

Electronic absorption spectra of the dendrimer and micelle were measured. DNPcZn exhibits strong Q band absorption at 780 nm, indicating successful dispersion as a monomeric species in the aqueous solution. According to the formation of the polyion

complex micelle, the absorption maximum of Q band absorption became broad, indicating the possibility of slight aggregate formation of the core naphthalocyanine units. The relatively small dendritic wedges may not perfectly prevent the aggregate formation of the naphthalocyanine core units especially in the densely packed micellar core. The absorption of light by tissue increases as the wavelength decreases and that the most efficient photosensitizers are those that have strong absorption bands between 600-800 nm. Therefore, although the relatively small dendritic wedges may not perfectly prevent collisional quenching, DNPcZn has the potential for use as an effective photosensitizer in photodynamic therapy.

Conclusions

The first example of polyion complex micelle formation of DNPcZn was demonstrated. DNPcZn/m exhibited long wavelength absorption around 750 nm, which is very advantageous for the treatment of deep lesions, because the long wavelength light is less absorbed by melanin dyes in skin tissue or heme proteins in blood. Furthermore, the micellar formulation may improve the longevity in blood circulation that achieves cumulative accumulation in the lesion with hyperpermeability, such as a macular degeneration, due to the Enhanced Permeation and Retention (EPR) effect [6]. The PDT efficacy of DPcZn/m is now under investigation in our research group.

Acknowledgement

This work was supported by Core Research Program for Evolutional Science and Technology (CREST) from Japan Science and Technology Agency and Center for Bioactive Molecular Hybrids (CBMH) from Korea Science and Engineering Foundation.

References

[1] IJ Macdonald, TJ Dougherty: *J. Porphyrins Phthalocyanines 5*(2) (2001), p.105.

[2] WD Jang, N Nishiyama, GD Zhang, A Harada, DL Jiang, S Kawauci, Y Morimoto, M Kikuchi, H Koyama, T Aida, and K Kataoka: *Angew. Chem. Int. Ed. 44*(3) (2005), p. 419.

[3] R Ideta, F Tasaka, WD Jang, N Nishiyama, GD Zhang, A Harada, Y Yanagi, Y Tamaki, T Aida, and K Kataoka: *Nano Lett. 5*(12) (2005), p. 2426.

[4] Y Kakizawa, K Kataoka: *Adv. Drug Delivery Rev. 54*(2) (2002), p. 203.

[5] A Harada, K Kataoka: *Macromolecules 28*(15) (1995), P. 5294.

[6] H Maeda, J Wu, T Sawa, Y Matsumura, K Hori: *J. Control. Release, 65*(1-2) (2000), p. 271.

Density Control of Poly(ethylene glycol) Layer To Regulate Cellular Attachment

Tomomi Satomi,[†,‡,§,∥] Yukio Nagasaki,[⊥] Hisatoshi Kobayashi,[§] Hidenori Otsuka,[*,†,‡,§] and Kazunori Kataoka[∥,#]

Department of Applied Chemistry, Faculty of Science, Tokyo University of Science, 1-3 Kagurazaka, Shinjuku-ku, Tokyo 162-8601, Japan, Division of Bioengineering and Bioinformatics, Graduate School of Information Science and Technology, Hokkaido University, North 14 West 9, Sapporo 060-0814, Japan, Biomaterials Center, National Institute for Materials Science (NIMS), 1-1 Namiki, Tsukuba, Ibaraki 305-0044, Japan, Division of Clinical Biotechnology, Center for Disease Biology and Integrative Medicine, Graduate School of Medicine, The University of Tokyo, 7-3-1 Hongo, Bunkyo-ku, Tokyo 113-0033, Japan, Graduate School of Pure and Applied Sciences, University of Tsukuba, 1-1-1 Tenodai, Tsukuba, Ibaraki 305-8571, Japan, and Department of Materials Science and Engineering, Graduate School of Engineering, The University of Tokyo, 7-3-1 Hongo, Tokyo 113-8656, Japan

Received August 17, 2006. In Final Form: March 7, 2007

A wide variety of cells usually integrate and respond to the microscale environment, such as soluble protein factors, extracellular matrix proteins, and contacts with neighboring cells. To gain insight into cellular microenvironment design, we investigated two-dimensional microarray formation of endothelial cells on a micropatterned poly(ethylene glycol) (PEG)-brushed surface, based on the relationship between PEG chain density and cellular attachment. The patterned substrates consisted of two regions: the PEG surface that acts as a cell-resistant layer and the exposed substrate surface that promotes protein or cell adsorption. A PEG-brushed layer was constructed on a gold substrate using PEG with a mercapto group at the end of the chain. The density of the PEG-brushed layer increased substantially with repetitive adsorption/rinse cycles of PEG on the gold substrate, allowing marked reduction of nonspecific protein adsorption. These repeated adsorption/rinse cycles were further regulated by using longer (5 kDa) and shorter (2 kDa) PEG to construct PEG layers with different chain density, and subsequent micropatterning was achieved by plasma etching through a micropatterned metal mask. The effects of PEG chain density on pattern formation of cell attachment were determined on micropatterning of endothelial cells. The results indicated that cell pattern formation was strongly dependent on the PEG chain density and on the extent of protein adsorption. Notably, a PEG chain density high enough to inhibit outgrowth of endothelial cells from the cell-adhering region in the horizontal direction could be obtained only by employing formation of a short filler layer of PEG in the preconstructed longer PEG-brushed layer, which prevented nonspecific protein adsorption almost completely. In this way, a completely micropatterned array of endothelial cells with long-term viability was obtained. This clearly indicated the importance of a short underbrushed PEG layer in minimizing nonspecific protein adsorption for long-term maintenance of the active cell pattern. The strategy for cell patterning presented here can be employed in tissue engineering to study cell−cell and cell−surface interactions. It is also applicable for high-throughput screening and clinical diagnostics, as well as interfacing cellular and microfabricated components of biomedical microsystems.

Introduction

Surface engineering techniques for cellular micropatterning are emerging as important tools to clarify the effects of the microenvironment on cellular behavior,[1,2] as cells usually integrate and respond to the microscale environment, such as chemical and mechanical properties of the surrounding fluid and extracellular matrix, soluble protein factors, small signal molecules, and contacts with neighboring cells.[3,4] Furthermore, living cells undergo physiological changes in response to exposure to drugs and environmental perturbations, such as toxins, pathogens, or other agents, and thus high-throughput technologies using whole cells have also been developed.[5−13] To develop this kind of cellular microarray composed of a cell-resistant surface and cell attachment region, micropatterning a protein-repellent surface is important because cellular adhesion and proliferation are regulated by protein adsorption.

* Corresponding author. Address: Hidenori Otsuka, Ph.D., Department of Applied Chemistry, Faculty of Science, Tokyo University of Science, 1-3 Kagurazaka, Shinjuku-ku, Tokyo 162-8601, Japan. Phone: +81-3-5228-8265. Fax: +81-3-5228-8265. E-mail: h.otsuka@rs.kagu.tus.ac.jp.

† Tokyo University of Science.

‡ Hokkaido University.

§ National Institute for Materials Science.

∥ Graduate School of Medicine, The University of Tokyo.

⊥ University of Tsukuba.

Graduate School of Engineering, The University of Tokyo.

(1) Whitesides, G. M.; Ostuni, E.; Takayama, S.; Jiang, X.; Ingber, D. E. *Annu. Rev. Biomed. Eng.* **2001**, *3*, 335.

(2) Jeon, N. L.; Baskaran, H.; Detringer, S. K. W.; Whitesides, G. M.; Van de Water, L.; Toner, M. *Nat. Biotechnol.* **2002**, *20*, 826.

(3) Zamir, E.; Katz, B. Z.; Aota, K. M.; Yamada, K. M.; Geiger, B.; Kam, Z. *J. Cell Sci.* **1999**, *112*, 1655.

(4) Geiger, B.; Bershadsky, R.; Pankov, R.; Yamada, K. M. *Nat. Rev. Mol. Cell Biol.* **2001**, *2*, 793.

(5) Stenger, D. A.; Gross, G. W.; Keefer, E. W.; Shaffer, K. M.; Andreadis, J. D.; Ma, W.; Pancrazio, J. J. *Trends Biotechnol.* **2001**, *19*, 304.

(6) Kononen, J.; Bubendorf, L.; Kallioniemi, A.; Barlund, M.; Schraml, P.; Leighton, S.; Torhorst, J.; Mihatsch, M. J.; Sauter, G.; Kallioniemi, O. P. *Nat. Med.* **1998**, *4*, 844.

(7) Ziauddin, J.; Sabatini, D. M. *Nature* **2001**, *411*, 107.

(8) Michalopoulos, G. K.; DeFrances, M. C. *Science* **1997**, *276*, 60.

(9) Anderson, D. G.; Levenberg, S.; Langer, R. *Nat. Biotechnol.* **2004**, *22*, 863.

(10) Revzin, A.; Tompkins, R. G.; Toner, M. *Langmuir* **2003**, *19*, 9855.

(11) Thielecke, H.; Mack, A.; Robitzki, A. *Biosens. Bioelectron.* **2001**, *16*, 261.

(12) Mack, A. R.; Thielecke, H.; Robitzki, A. A. *Trends Biotechnol.* **2002**, *20*, 56.

(13) Otsuka, H.; Hirano, A.; Nagasaki, Y.; Okano, T.; Horiike, Y.; Kataoka, K. *ChemBioChem* **2004**, *5*, 850.

10.1021/la0624384 CCC: $37.00
Published on Web 05/05/2007

A number of approaches to construct protein-repellent and subsequent cell-repellent surfaces have been studied using polymer coating. In fact, there has been a great deal of discussion regarding the molecular properties on the surface, and it is widely believed that effective protein rejection requires the bound polymer to be heavily hydrated, densely packed, neutral, deposited in a thick layer, and conformationally mobile.[14-18] Here, we focus on poly(ethylene glycol) (PEG), one of the most useful polymers to repel protein. Surface modification by PEG leads to a significant reduction in the nonspecific interaction of biological molecules with the surface due to its high degree of hydrophilicity and chain flexibility, inducing an effective exclusion volume effect.[19-22] Most previous studies of surfaces with immobilized PEG have described higher protein-repellent ability with longer chain, resulting in increasing thickness of PEG,[23-27] which is considered to be due to the stronger attenuation of the long-range Lifshitz–van der Waals attraction. However, immobilization of longer PEG chains results in a decrease in chain density due to its larger exclusion volume effect, although it has a sufficiently large separation between the surface and proteins. Conversely, immobilization of shorter PEG chains gives higher density due to its smaller exclusion volume effect, although it has a smaller separation between the surface and proteins. To resolve this controversial issue of the length and density of the PEG layer, we previously reported the development of surface construction using long and short PEG chains; formation of a short, filler layer of PEG in the preconstructed longer PEG-brushed layer prevented nonspecific protein adsorption almost completely.[28] In most studies of this type, a protein-repellent surface will be expected to repel cellular attachment. However, the question of how dense the immobilized PEG chain must be to control cell attachment has still not been answered.

The present study was performed to determine the influence of PEG chain density on cellular attachment directly. For the micropatterning of cells, it is necessary to prevent overgrowth of cells from the cell-adhering pattern; i.e., construction of a cytophobic surface is important for micropatterning. Here, we controlled the modification ratio of long and short PEG chains to construct surfaces with different PEG chain densities, and subsequent micropatterning was achieved by plasma etching through a micropatterned metal mask (ϕ = 100 μm, edge-to-edge spacing of l = 300 μm). The relationship between PEG chain density and cellular attachment is discussed on micropatterning of endothelial cells.

(14) Lee, J. H.; Kopeckova, P.; Kopecek, J.; Andrade, J. D. *Biomaterials* **1990**, *11*, 455.
(15) Desai, N. P.; Hubbell, J. A. *Macromolecules* **1992**, *25*, 226.
(16) Bergstrom, K.; Osterberg, E.; Holmberg, K.; Riggs, J. A.; Van Alstime, J. M.; Schuman, T. P.; Burns, N. L.; Harris, J. M. *Colloids Surf. A* **1993**, *77*, 159.
(17) Sofia, S. J.; Premnath, V.; Merrill, E. W. *Macromolecules* **1998**, *31*, 5059.
(18) Osterberg, E.; Bergstrom, K.; Holmberg, K.; Schuman, T. P.; Riggs, J. A.;. Burns, N. L; Van Alstine, J. M.; Harris, J. M. *J. Biomed. Mater. Res.* **1995**, *29*, 741.
(19) Mori, Y.; Nagaoka, S.; Takiuchi, H.; Kikuchi, T.; Noguchi, N.; Tanzawa, H.; Noishiki, Y. *Trans. Am. Soc. Artif. Internal Organs* **1982**, *28*, 459.
(20) Bergstrom, K.; Osterberg, E.; Holmberg, K.; Hoffman, A. S.; Schuman, T. P.; Kozlowski, A.; Harris, J. M. *J. Biomater. Sci. Polym. Ed.* **1994**, *6*, 123.
(21) Harris, J. M., Ed. *Poly(ethylene glycol) Chemistry. Biotechnical and Biomedical Applications*; Plenum Press: New York, 1992.
(22) Glass, J. E., Ed. *Hydrophilic Polymers. Performance with Environmental Acceptance*; American Chemical Society: Washington DC, 1996.
(23) Prime, K. L.; Whiteside, G. M. *J. Am. Chem. Soc.* **1993**, *115*, 10714.
(24) Gombotz, W. R.; Guanghui, W.; Horbett, T. A.; Hoffman, A. S. *J. Biomed. Mater. Res.* **1991**, *25*, 1547.
(25) Lee, J.; Martic, P. A.; Tan, J. S. *J. Colloid Interface Sci.* **1989**, *131*, 252.
(26) Jeon, S. I.; Andrade, J. D.; de Gennes, P. G. *J. Colloid Interface Sci.* **1991**, *142*, 159.
(27) Roosjen, A.; van der Mei, H. C.; Busscher, H. J.; Norde, W. *Langmuir* **2004**, *20*, 10949.
(28) Uchida, K.; Otsuka, H.; Kaneko, M.; Kataoka, K.; Nagasaki, Y. *Anal. Chem.* **2005**, *77*, 1075.

Experimental Section

Materials. Poly(ethylene glycol) (PEG) with a methoxy group at one end and a mercapto group at the other (MeO–PEG–SH) was provided by NOF Corporation (Tokyo, Japan). The molecular weight and polydispersity of PEGs, denoted by PEG2k and PEG5k, were 2096 and 1.05 and 5341 and 1.04, respectively. Gold chips (SIA KIT Au) for SPR measurements were purchased from Biacore AB (Uppsala, Sweden). Human umbilical endothelial cells (HUVEC) were purchased from Cambrex (Cambrex BioScience Walkersville, Inc., Walkersville, MD). HUVECs were cultured in EBM-2 medium (Cambrex). Water used in this study was purified by passing it through a Milli-Q System (Nihon Millipore Co., Tokyo, Japan) until its specific conductivity fell below 0.1 μS cm^{-1}.

1. PEG Immobilization Study. *Preparation of MeO–PEG–SH-Modified Gold Surface.* Immobilization of PEG on the gold sensor chip surface was performed using a surface plasmon resonance (SPR) instrument (Biacore X; Biacore AB, Uppsala, Sweden). Phosphate buffered saline (PBS; pH 7.4, 0.15 M, containing 1 M NaCl) solutions of PEG were injected at a flow rate of 10 μL/min for 10 min at 37 °C under running PBS (pH 7.4, 0.15 M, containing 1 M NaCl). An SPR sensorgram on the gold sensor chip for this adsorption/rinsing (with running PBS) of PEG was monitored, and the amount of immobilized PEG was assessed by the SPR angle shift. PEG solutions with different concentrations were injected on a sensor chip, and then the plateau region for PEG immobilization was determined. To increase (or change) the amount of immobilized PEG, the process of PEG injection was repeated several times according to the reported method.[24] PEGylated surfaces prepared by one, two, and three repetitive injections were denoted as PEG5k(1), PEG5k(2), and PEG5k(3) surfaces, respectively. In a manner similar to the above-repeated process, successive PEGylation with longer and then shorter PEG was carried out. A shorter PEG (PEG2k) as a filler was layered on the surface with the preconstructed longer PEG brushes (PEG5k) by repetitive injection. PEG5k(1) surfaces with three treatments with the filler PEG and PEG5k(2) with four treatments with the filler PEG were denoted as PEG5k(1)/2k(3) and PEG5k(2)/2k(4) surfaces, respectively.

The density of immobilized PEG chains was estimated quantitatively by quartz crystal microbalance (QCM) measurement using an AT-cut gold-sputtered quartz crystal with a resonance frequency of 27 MHz (Initium Inc., Japan). The frequency was recorded after immersing the crystals in the PBS (pH 7.4, 0.15 M, containing 1 M NaCl) at 37 °C. After baseline stabilization, PEG solutions (PEG5k, PEG2k) were injected at a concentration of 0.01 mg/mL, which was optimized above in the same repetitive manner as in SPR measurement (PEG5k(3), PEG5k(1)/2k(3), PEG5k(2)/2k(4)).

Surface Characterization. The wettability of all PEGylated surfaces was estimated from the static and dynamic contact angle measurements (CA-W contact angle meter; Kyowa Interface Science Co., Ltd., Tokyo, Japan).[29] Gold and PEGylated gold surfaces were constructed on glass substrates as described in detail in the section describing the cell culture study (see "Construction of PEGylated surface"). Water-in-air and air-in-water systems were applied in the static contact angle measurements. Water-in-air system measurement was performed by a sessile droplet technique, where a water droplet (Milli-Q quality) was placed on the sample surface at 25 °C. The air-in-water system procedure followed the captive bubble technique, where the sample surface was immersed in water maintained at 25 °C and a small air bubble was placed on the sample surface from the bottom using a curved needle. The contact angle of each surface was measured on 10 spots, and the obtained values were averaged.

For dynamic contact angle measurements, the advancing (θ_{adv}) and receding (θ_{rec}) contact angles were obtained by extending and then contracting the volume (5.9 μL) of the water droplet using a motor-driven syringe at a rate of 1.88 μL/s for 3.1 s. The extending/contracting droplet was monitored with a CCD camera; each picture was captured every 67 ms, and 24 images were taken for both θ_{adv} and θ_{rec}, when the water droplet volume was changed at 1.88 μL/s. The contact angles were evaluated from video printouts of the droplet.

(29) Otsuka, H.; Nagasaki, Y.; Kataoka, K. *Biomacromolecules* **2000**, *1*, 39.

Protein Adsorption Study. A protein adsorption study, which is an important reference for cell attachment, was performed using SPR equipment. Before the protein adsorption study, three types of PEGylated surface were constructed on a gold sensor chip in the same manner as described above: PEG5k(3), PEG5k(1)/2k(3), and PEG5k(2)/2k(4). And then protein adsorption was estimated by flowing 100 μL of serum-containing medium (EBM-2 medium to culture HUVEC) at a flow rate of 10 μL/min at 37 °C under running PBS (pH 7.4, 0.15 M) on the three types of PEGylated surface and native gold surface. The magnitude of the SPR angle shift by this injection was measured from the data taken from the final part of the curve after the surfaces were rinsed, and assessed as the amount of protein adsorbed. As a control, protein adsorption on a bare gold surface was examined.

2. Cell Culture Study. *Construction of PEGylated Surface.* Glass slides were etched with a boiling mixture of 50% (v/v) sulfuric acid and 50% (v/v) hydrogen peroxide for 30 min and then rinsed thoroughly with water. At 10^{-6} Torr, a 10 Å film of chromium was vapor-deposited at a rate of 0.1 Å/s onto the glass substrate. A 200 Å film of gold was then vapor-deposited on top of it at a rate of 0.1 Å/s. PEGylated surfaces were prepared on the gold films in the same manner as described for SPR measurements. PBS (pH 7.4, 0.15 M, containing 1 M NaCl) solutions of PEG5k (0.01 mg/mL) and PEG2k (0.01 mg/mL) were prepared. Then, PEG solutions with the appropriate conditions were retained on the gold film for 30 min to construct the PEGylated surfaces described above (PEG5k(3), PEG5k(1)/2k(3), PEG5k(2)/2k(4)). The plates were washed with Milli-Q water between each PEGylation, for 5 min each time.

Micropatterning of PEGylated Surface. The micropattern on the PEGylated surfaces were obtained by $N_2 + H_2$ plasma etching using a metal mask with holes 100 μm in diameter spaced 300 μm apart. After construction of a 2-well plastic chamber (Falcon BD) on the glass thus prepared, all samples were sterilized with ethylene oxide gas.

Cell Culture Study. HUVECs were seeded onto the micropatterned PEGylated surface at a cell density of 1×10^6 cells/mL. Cells were cultured at 37 °C in a humidified atmosphere of 5% CO_2. An EBM-2 medium was used for cultivation and was exchanged every 2 days.

Results and Discussion

Micropatterned PEGylated substrates with two-dimensional arrays of plasma-etched circular domains (ϕ = 100 μm) were prepared by sequential immobilization of PEG possessing a mercapto group at the end of the chain on the gold substrate, followed by plasma etching through a metal mask pattern with circular holes. The PEGylated region on the patterned substrate acts to repel proteins and thus inhibits cell adhesion. Proteins are expected to adsorb from the serum-containing medium onto the plasma-etched circular domains, exposing the base gold surface.

1. PEG Immobilization Study. The surface properties of the PEG coating were studied in detail to estimate protein adsorption and subsequent cell culture study on PEGylated surfaces. First, PBS solutions of various concentrations of PEG including 1 M NaCl were injected onto the gold surface using an SPR instrument to optimize immobilized concentration on a sensor chip. Use of high ionic strength buffer caused an increase in the amount of immobilized PEG, due to the appreciably reduced solubility of PEG in concentrated buffer solution.[30] The changes in SPR angle at each concentration of PEG5k are plotted in Figure 1. The results confirmed that the amount of immobilized PEG increased with increases in the injected PEG concentration; saturation was observed at PEG concentrations over 0.01 mg/mL, suggesting that the amount of possible immobilization on the gold surface is constant with injection of PEG above this concentration. There were no significant differences in this PEG immobilization study between PEG2k and PEG5k. Therefore, immobilization of PEG

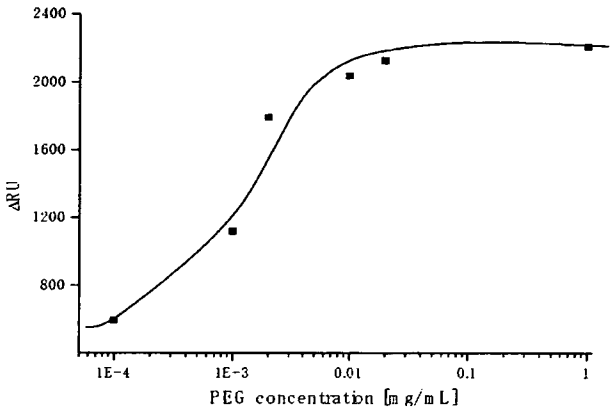

Figure 1. PEG immobilization as a function of PEG concentration. Flow rate, 10 μL/min; running buffer, PBS (pH 7.4, 0.15 M, containing 1 M NaCl); sample, PEG (M_w: 5k)/PBS (0.15 M, pH 7.4, containing 1 M NaCl) solution; sample injection, 100 μL.

on the gold surface was performed with 0.01 mg/mL PEG solution. Three types of PEG immobilization (PEG5k(3), PEG5k(1)/2k-(3), PEG5k(2)/2k(4), as described in the experimental section) were performed at this concentration, as shown in SPR sensorgrams (Figure 2). After first treatment with PEG5k, the sensor surface was washed under running buffer to remove noncovalently adsorbed PEG. The sensor chip was then treated again with a solution of PEG5k. This cycle of adsorption/rinsing of PEG5k was repeated several times. Eventually, the total SPR angle shift was amplified by increasing the number of treatment cycles to three, indicating that repetitive treatment with PEG5k was effective in increasing the density of PEG (PEG5k(3)). Notably, this trend became even more significant following additional treatment of the PEG5k surface with shorter PEG (PEG2k), as shown in Figure 2b,c. We planned to increase the surface brush density by PEG2k, retaining the PEG5k brush surface character. Sensorgrams showed a number of interesting findings. First, immobilization of long-chain PEG (PEG5k(1)) increased markedly with changes in SPR angle (Figure 2a–c). However, the extent of the shift decreased with the second injection of long-chain PEG (PEG5k(2)) (Figure 2a,c), and little change was seen on the third injection of long-chain PEG (PEG5k-(3)) (Figure 2a). On the other hand, immobilization of short-chain PEG (PEG2k(1)) after long-chain PEG resulted again in marked changes (Figure 2b,c). These results suggested that long-chain PEG5k can hardly penetrate into the preconstructed longer PEG-brushed layer due to its exclusion volume effect, while short-chain PEG2k appreciably filled the gap in the preconstructed longer PEG layer. It should be noted that SPR sensorgrams showed a steep increase curve in PEG2k(1), as shown in Figure 2b,c, indicating the importance of a short underbrushed PEG layer in increasing the PEG chain density.

To confirm that these SPR angle changes are reflected directly in the amount of immobilized PEG, QCM measurement was performed in the same manner as SPR (Table 1). The average value of total frequency shift after PEG injection is given as Δf in Table 1. PEG5k(2)/2k(4) surface showed the largest frequency shift, and PEG5k(1)/2k(3) surface also showed around 2000 Hz in frequency shift. On the other hand, PEG5k(3) surface showed around 1400 Hz in total frequency shift. Thus, PEG5k surface mixed with PEG2k showed larger mass change than only PEG5k chain immobilization, which suggested that more PEG chains were immobilized in PEG5k and PEG2k mixed surface. This result also indicated a significant role of a short underbrushed PEG layer in increasing the PEG chain density. On QCM

(30) Emoto, K.; Harris, J. M.; Alstine, M. V. *Anal. Chem.* **1996**, *68*, 3751.

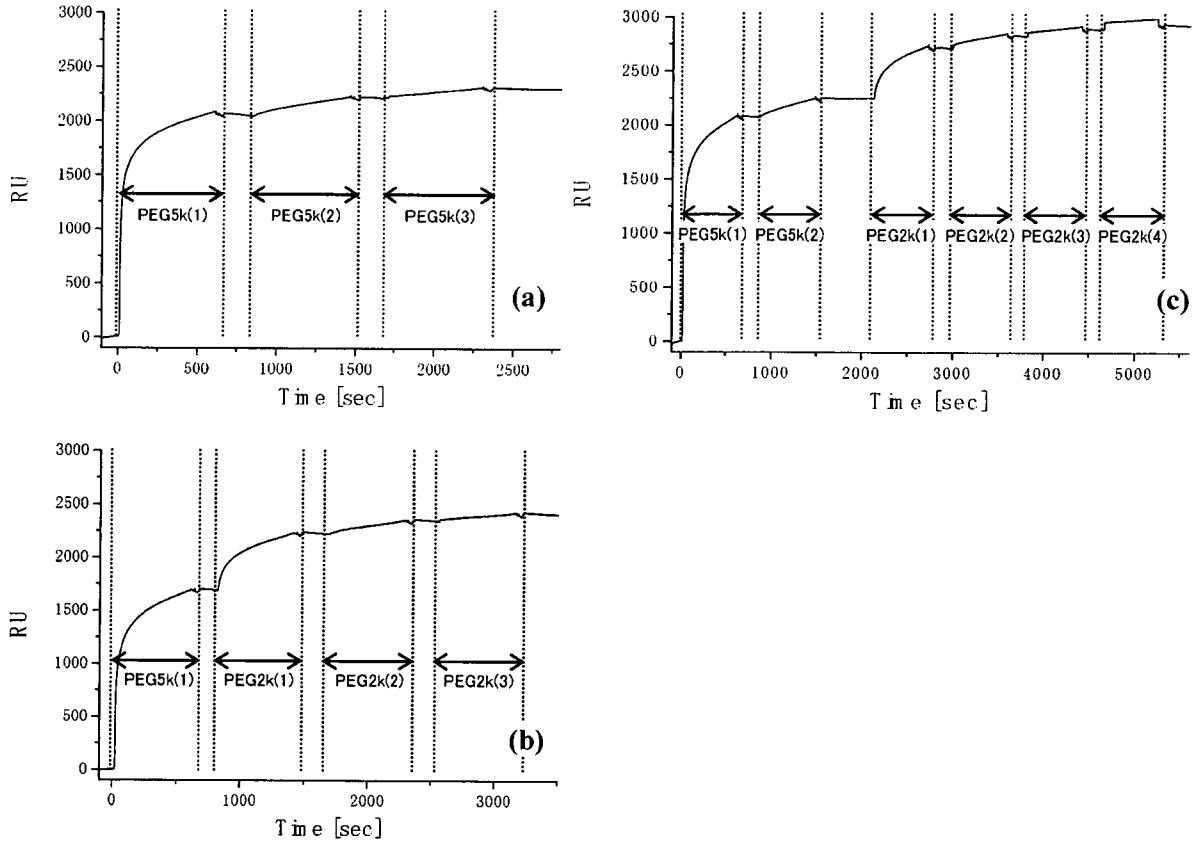

Figure 2. Sensorgrams of PEG immobilization on gold surfaces. (a) PEG5k(3), (b) PEG5k(1)/2k(3), and (c)PEG5k(2)/2k(4). Flow rate, 10 μL/min; running buffer, PBS (0.15 M, pH 7.4, containing 1 M NaCl); sample, 0.01 mg/mL of PEG (M_w: 5k or 2k)/PBS (0.15 M, pH7.4, containing 1 M NaCl) solution; sample injection, 100 μL for each time point.

Table 1. Comparison of Three Types of PEG Immobilization Measured by QCM: Δf is the Average of Total Frequency Shift after PEG Immobilization (n = 3)

PEG surfaces	Δf(Hz)	±S.D.
5k(3)	1382.8	118.6
5k(1)/2k(3)	1922.8	92.70
5k(2)/2k(4)	2144.7	81.74

measurement, the PEG5k(2)/2k(4) surface was determined to have the highest PEG chain density, while PEG5k(3) had the lowest.

The static wettability of the surface coated with PEG was estimated in both air and water by contact angle measurement (Figure 3). In the water-in-air measurement, the coating of PEG on the gold substrate significantly increased its wettability, as indicated by a decrease in the static contact angle (~30°). A similar trend was observed in the air-in-water measurement and the effect of PEG density on wettability was more pronounced, showing progressively increasing contact angle with increasing PEG chain density. Note that the increase in contact angle corresponds to an increase in wettability for the air-in-water system. As the accuracy of contact angle is ±2°, as shown by Zisman and co-worker,[31] significant differences could be seen between PEG surfaces. Furthermore, advancing/receding contact angles and hysteresis were measured on each PEG surface to estimate the dynamics of the uppermost surface in detail (Figure 4). In receding contact angles, each PEG surface showed a small value of around 15−20° and there was little difference between surfaces. On the other hand, critical differences were observed

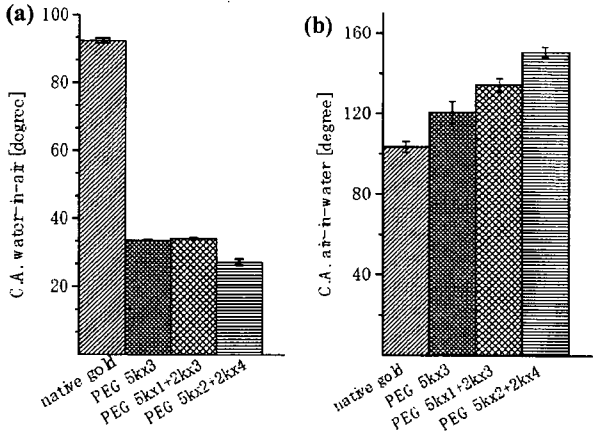

Figure 3. Static water contact angles on PEGylated gold surface. (a) Water-in-air system; (b) air-in-water system.

in advancing contact angles. PEG5k(3) and PEG5k(1)/2k(3) surfaces had around 30°, while the value for the PEG5k(2)/2k(4) surface was almost half. As PEG surfaces are easy to hydrate and show good water retentivity, once they became wet, receding contact angles showed small values in all PEG surfaces, resulting in little difference in receding contact angle. In contrast, significant differences were observed in advancing contact angles, indicating that the PEG5k(2)/2k(4) surface has the greatest wettability in the dry to wet state as compared with the other PEG surfaces examined. Hysteresis indicated differences between PEG5k(2)/2k(4) surfaces and the other surfaces according to its high surface free energy. When the water droplet extends, the surface with

(31) Fox, H. W.; Zisman, W. A. *J. Colloid Sci.* **1950**, *5*, 514.

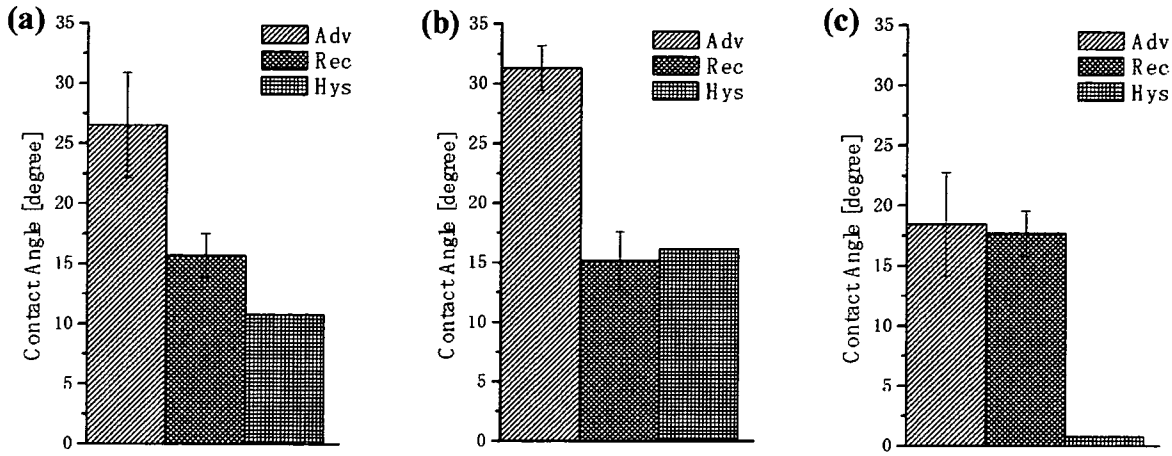

Figure 4. Dynamic water contact angles on PEGylated gold surfaces. (a) PEG5k(3), (b) PEG5k(1)/2k(3), and (c) PEG5k(2)2k(4).

a high surface free energy facilitates penetration of water, aiding in water droplet spreading, while the surface prevents the water droplet from receding when it contracts. Accordingly, the observations of the present study suggested that the PEG5k-(2)/2k(4) surface is the most hydrophilic and has a high surface free energy due to its high PEG chain density. Furthermore, the chain density is reported to have the relation with other parameters including the thickness and conformation of PEG layer.[23-27,32,33] The PEG chains (5k and 2k) are more well-oriented in this surface since the short, filler-like PEG2k chains will enhance the lateral interactions (e.g., hydrogen bonding and van der Waals force) between the PEG chains. This will likely result in much enhanced water affinity/penetration capability in PEG chains during the advancing angle measurement. Therefore, only small hysteresis value will be found on a PEG5k(2)/2k(4) surface.

Nonspecific protein adsorption from the culture medium for HUVEC was estimated on each PEG-coated surface to estimate the cytophobicity of PEGylated surfaces because the adsorbed proteins are responsible for subsequent cell adhesion. On bare gold as a control, the SPR angle shift due to the nonspecific adsorption of protein was 2927.4 RU, when a serum-containing cell (HUVEC) culture medium (EBM-2) was passed over the surface for 10 min at a flow rate of 10 μL/min. In contrast, PEG-coated surfaces clearly reduced protein adsorption (Figure 5). Figure 5 also shows a comparison of protein adsorption on the three types of PEG surface. The SPR angle shift was 676.5, 350.8, and 218.0 RU on PEG5k(3), PEG5k(1)/2k(3), and PEG 5k(2)/2k(4) surfaces, respectively. The PEG5k(2)/2k(4) surface showed the greatest degree of inhibition of protein adsorption from the medium, suggesting that the inhibitory effect of nonspecific protein adsorption was the highest for this surface among those studied. The physicochemical properties of PEG surfaces described above indicate that PEG surfaces with higher immobilized PEG chain density have greater ability to repel proteins. Based on these results, it was concluded that shorter PEG, viz. an underbrushed layer to increase the PEG surface density, played a substantial role in minimizing nonspecific protein adsorption. Other workers have also proposed that PEG mixtures, which are polydisperse with respect to molecular weight, are more efficacious than single molecular weights. Mixed PEGs were shown to have greatest efficacy in steric stabilization of colloidal particles and in protein repellency.[34,35] The PEG5k-

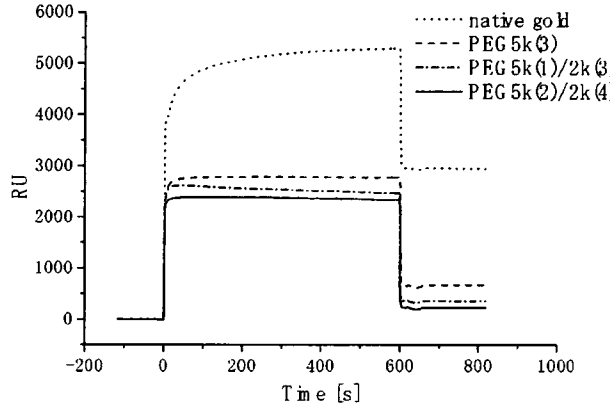

Figure 5. Sensorgrams of injection of serum-containing cell culture medium (EBM-2 medium to culture HUVEC) on native gold and each PEGylated surfaces. Flow rate, 10 μL/min; running buffer, PBS (pH 7.4, 0.15 M); sample injection volume, 100 μL.

(2)/2k(4) surface with the highest PEG chain density was expected to have the highest cytophobicity.

2. Cell Culture Study. Gold surfaces were coated with PEG to inhibit nonspecific protein adsorption and were expected to act as cytophobic surfaces for subsequent cell patterning. The PEG-coated gold substrates were micropatterned by plasma etching ($N_2 + H_2$) through a metal mask pattern with ϕ100 μm circular holes separated by 300 μm (edge-to-edge distance), and cell culture dishes were then set onto these surfaces (2 × 2 cm). Microscopic images following seeding of HUVEC on the surfaces are shown in Figure 6. On PEG5k(3) surfaces with lower PEG chain density as suggested by physicochemical studies, seeded HUVEC showed disorganized cellular attachment regardless of micropatterned substrate (Figure 6a). On the other hand, the PEG5k(1)/2k(3) surface (Figure 6b) and PEG5k(2)/2k(4) surface (Figure 6c) showed patterned cell attachment due to the suggested higher PEG chain density compared with that of the PEG5k(3) surface, although cells that had overgrown beyond the pattern were still observed on PEG5k(1)/2k(3) surfaces. The results of cultivation of HUVECs for 1 week are shown in Figure 6d–f. Arrayed cellular attachment was observed only on the PEG5k-(2)/2k(4) surface (Figure 6f). In contrast, the HUVECs began to bridge across multiple islands on the PEG5k(1)/2k(3) surface (Figure 6e) and this bridging was more pronounced to form a complete cell sheet on the PEG5k(3) surface (Figure 6d). It is

(32) Harder, P.; Grunze, M.; Dahint, R.; Whitesides, G. M.; Laibinis, P. E. *J. Phys. Chem.* **1998**, *102*, 426.
(33) Zhu, B.; Eurell, T.; Gunawan, R.; Leckband, D. *J. Biomed. Mater. Res.* **2001**, *56*, 406.
(34) Stenkamp, V. S.; Berg, J. C. *Langmuir* **1997**, *13*, 3827.
(35) Pavey, K. D.; Olliff, C. J. *Biomaterials* **1999**, *20*, 885.

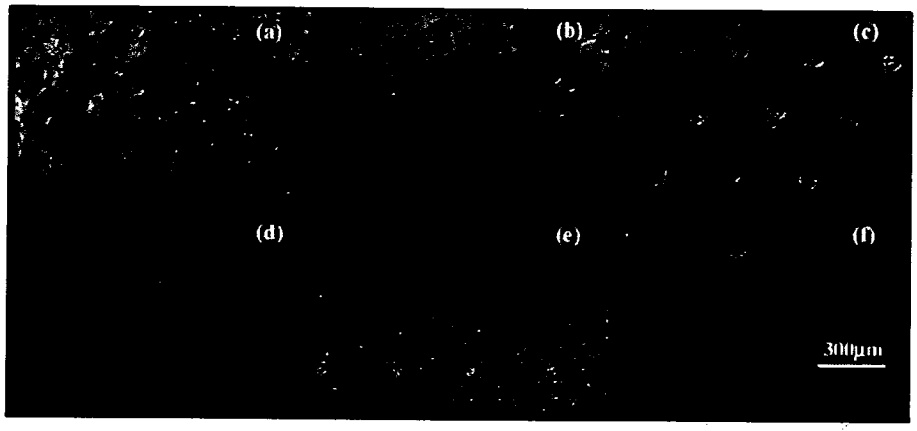

Figure 6. Microscopic image of cell seeding study. After 1 day of culture of HUVEC on micropatterned (a) PEG5k(3) surface, (b) PEG5k-(1)/2k(3) surface, and (c) PEG5k(2)/2k(4) surface. After 1 week of culture of HUVEC on micropatterned (d) PEG5k(3) surface, (e) PEG5k-(1)/2k(3) surface, and (f) PEG5k(2)/2k(4) surface.

clear that PEG chain density affects pattern recognition in cell attachment. The threshold density for HUVEC bridging seems to exist on the surface between PEG5k(3) and PEG5k(2)/2k(4). Cells overgrew beyond the pattern on weak protein-repellent surfaces. In addition, when overgrown cells grew sufficiently close together, bridging occurred between overgrown cellular patterns. Attached patterns eventually resulted in sheet formation. As described above, no pattern recognition of cell attachment was seen on the surfaces coated only with long-chain PEG (PEG5k(3)) because of its lower inhibitory effect on nonspecific protein adsorption. In contrast, cell array formation was observed by constructing long- and short-chain PEG mixed surfaces. Furthermore, PEG5k(2)/2k(4) surfaces showed the least non-specific cell attachment in contrast to some nonspecific cell attachment and bridging of cellular islands on PEG5k(1)/2k(3) surfaces. SPR results indicated that cell-adhesive proteins are greatly repelled on PEG5k(2)/2k(4) surfaces to promote pattern recognition of cell attachment. Some cell attachment between cellular islands was confirmed on PEG5k(3) and 5k(1)/2k(3) surfaces after 1 day in culture, and the attached cells extended toward each other and bridging occurred across cellular islands. Bridged cellular patterns grew everywhere on the surface and eventually formed a complete cell sheet. As the first cell attachment on the cytophobic region depends on the ability of the surface to repel protein, surfaces with lower PEG chain density (PEG5k(3) or PEG5k(1)/2k(3)) resulted in cell attachment and cell sheet formation. Thus, the results of the cell culture study agreed well with the surface properties, suggesting that PEG chain density played a critical role in micropatterned cell attachment.

Conclusions

To gain insight into the design of cellular microenvironments, we examined the micropatterning of endothelial cells on microfabricated gold substrates coated with PEG brushes in terms of the relationship between PEG chain density and cellular attachment. A PEG-brushed layer was constructed on a gold substrate using PEG with a mercapto group at the chain end. After treatment with longer chain PEG with a molecular weight of 5000, shorter chain PEG (2000) was introduced onto the gold substrate to modulate the chain density. In this way, PEGylated surfaces with different chain densities were produced, and subsequent micropatterning was achieved by plasma etching through a micropatterned metal mask. The results indicated that cell pattern formation was strongly dependent on both the PEG chain density and the extent of protein adsorption, as evidenced by physicochemical and biological characterization of PEGylated surfaces using SPR, QCM, and static/dynamic contact angle measurements. Cell micropatterning showed long-term retention only on the surfaces with greater disparity between cytophobic and cytophilic regions. Notably, a PEG chain density sufficiently high to inhibit outgrowth of endothelial cells beyond the cytophilic gold region to the cytophobic PEGylated region could be obtained only on the mixed PEG chain-tethered surface, which achieved almost complete prevention of nonspecific protein adsorption. These observations clearly indicated that shorter PEG, viz. an underbrushed PEG layer to increase the PEG surface density, played a substantial role in minimizing nonspecific protein adsorption and long-term maintenance of the active cell pattern. It should be noted that the precise control of surface properties in single-molecule order directly affected micropatterned cellular attachment. Therefore, we envision the cellular micropatterning technique presented here becoming a valuable tool for the control of cell−surface and cell−cell interactions on a micrometer scale and to evaluate local effects of engineered microenvironments on cellular behavior. The surface fabrication technique studied here is a promising technology for the development of tissue/cell-based biosensors and in the field of tissue engineering.

Acknowledgment. Microfabrication using the plasma etching technique was conducted at the National Institute for Materials Science (NIMS), Japan, with assistance from Dr. Y. Horiike. Financial support for this work was partly provided by Special Coordination Funds for Promoting Science and Technology and also supported by Research Promotion Bureau under contract nos. 15-99 and 15-396, both from the Ministry of Education, Culture, Sports, Science, and Technology (MEXT), Japan. Part of this work was also supported financially by a Grant-in-Aid for Research on Health Sciences for Drug Innovation (KH71066), Ministry of Health, Labor, and Welfare of Japan, and The New Energy and Industrial Technology Development Organization (NEDO).

LA0624384

Available online at www.sciencedirect.com
ScienceDirect
Colloids and Surfaces B: Biointerfaces 56 (2007) 174–181
COLLOIDS AND SURFACES B
www.elsevier.com/locate/colsurfb

Iron hydroxide nanoparticles coated with poly(ethylene glycol)-poly(aspartic acid) block copolymer as novel magnetic resonance contrast agents for *in vivo* cancer imaging

Michiaki Kumagai [a], Yutaka Imai [a,b], Teisaku Nakamura [a], Yuichi Yamasaki [a], Masaki Sekino [c], Shoogo Ueno [c], Kenjiro Hanaoka [d], Kazuya Kikuchi [d], Tetsuo Nagano [d], Eiji Kaneko [b], Kentaro Shimokado [b], Kazunori Kataoka [a,e,f,*]

[a] *Department of Materials Engineering, School of Engineering, The University of Tokyo, 7-3-1 Hongo, Bunkyo-ku, Tokyo 113-8656, Japan*
[b] *Department of Vascular Medicine and Geriatrics, School of Medicine, Tokyo Medical and Dental University, 1-5-45 Yushima, Bunkyo, Tokyo 113-8519, Japan*
[c] *Department of Biomedical Engineering, School of Medicine, University of Tokyo, 7-3-1 Hongo, Bunkyo-ku, Tokyo 113-0033, Japan*
[d] *School of Pharmaceutical Sciences, The University of Tokyo, 7-3-1 Hongo, Bunkyo-ku, Tokyo 113-0033, Japan*
[e] *Center for Disease Biology and Integrative Medicine, School of Medicine, The University of Tokyo, 7-3-1 Hongo, Bunkyo-ku, Tokyo 113-0033, Japan*
[f] *Center for NanoBio Integration, The University of Tokyo, 7-3-1 Hongo, Bunkyo-ku, Tokyo 113-8656, Japan*

Available online 18 January 2007

Abstract

PEG-coated β-FeOOH nanoparticles were prepared through electrostatic complex formation of iron oxide nanoparticles with poly(ethylene glycol)-poly(aspartic acid) block copolymer [PEG-P(Asp)] in distilled water. By dynamic light scattering (DLS) measurement, the nanopaticle size was determined to be 70 nm with narrow distribution. The FT-IR and zeta potential experimental results proved that PEG-PAsp molecules bound to the surface of the iron oxide nanoparticles via the coordination between the carboxylic acid residues in the PAsp segment of the block copolymer and the surface Fe of the β-FeOOH nanoparticles. The PEG-coated nanoparticles revealed excellent solubility and stability in aqueous solution as well as in physiological saline. *In vivo* MRI experiments on tumor-bearing mice demonstrated that the PEG-coated nanoparticles prepared by the current approach achieved an appreciable accumulation into solid tumor, suggesting their potential utility as tumor-selective MRI contrast agents.

Keywords: Magnetic resonance imaging; Tumor; Contrast agent; β-FeOOH; Poly(ethylene glycol); Block copolymer; Zeta potential; FT-IR

1. Introduction

Magnetic nanoparticles have been deemed to have a great potential in *in vivo* biomedical applications including magnetic resonance imaging (MRI) contrast enhancement [1–8], targeted drug delivery [9–12], hyperthermia [13,14], and magnetic field assisted radionuclide therapy [15]. In particular, magnetic nanoparticles can be utilized as magnetic probes with signal-enhancing capability, which can resolve the weakness of the current MRI techniques. Although MRI has been one of the most powerful medical diagnostic tools due to its non-invasive nature and multidimensional tomographic capabilities coupled with high spatial resolution, a low signal–noise ratio as medical diagnostic instrument limits its use to the elucidations of lesions within the body only in the order of 500 μm. This limitation of the instrument has facilitated the development of several types of contrast enhancement agents including magnetite/dextran-based nanoparticles, which are currently available on the market and clinically used for liver imaging [16]. However, magnetite/dextran-based nanoparticles preferentially accumulate into reticulo-endotherial systems [17,18], resulting in the poor availability in the imaging of other tissues and organs, particularly solid tumors. Therefore, it is essential to engineer the surface of the iron oxide nanoparticles to minimize biofouling and non-specific aggregation in physiological conditions (i.e., high salt and protein concentrations), allowing their blood circulation for the prolonged period of time to reveal the enhanced accumulation into solid tumors [19–21].

* Corresponding author at: Department of Materials Engineering, School of Engineering, The University of Tokyo, 7-3-1 Hongo, Bunkyo-ku, Tokyo 113-8656, Japan. Tel.: +81 3 5841 7138; fax: +81 3 5841 7139.
E-mail address: kataoka@bmw.t.u-tokyo.ac.jp (K. Kataoka).

0927-7765/$ – see front matter
doi:10.1016/j.colsurfb.2006.12.019

Several synthetic and natural polymers have been employed to modify the surface of the iron oxide nanoparticles to enhance their function *in vivo* [13]. These polymers include dextran [22,23], poly(ethylene glycol) (PEG) [10,20,24], and poly(vinylpyrrolidone) (PVP) [25], all of which are known to be biocompatible, and thus feasible to construct iron oxide nanoparticles with longevity in the blood circulation. Particularly, PEG-coating on iron oxide nanoparticles has been known to improve biocompatibility and blood circulation times [10,26,27]. Recently, the MR imaging of solid tumor has been demonstrated using iron oxide nanoparticles coated with PEG-silane copolymer [11]. And also, it has been demonstrated that maghemite nanoparticles coated with PEG-polyanion block copolymer via electrostatic interaction have a longer half-life in the blood stream compared to dextran-coated iron oxide nanoparticles, allowing the enhanced MR imaging of the liver by their intravenous administration [28,29]. Nevertheless, the relationship between the physicochemical surface properties of PEG-coated iron oxide nanoparticles and their *in vivo* performance as MR contrast agents have not so far been well-elucidated, motivating us to the present study focusing on this important subject.

As for the physicochemical characterization, the infrared spectra of the iron oxide nanoparticles coated with PEG-poly(aspartic acid) block copolymer (PEG-PAsp) with an appreciable biocompatibility were particularly highlighted here to get insight into the coordination mechanism of the block copolymer onto the Fe species of the nanoparticles. Although several types of iron oxide nanoparticles, such as Fe_3O_4, γ-Fe_2O_3, have already been investigated in the previous studies as MR contrast agents [30–33], none of the β-FeOOH nanoparticles have so far been studied as MR contrast agents despite of their unique characteristics such as magnetism [34] and progressive biodegradability at times of the order of 1 month [35]. This may be a good reason to focus on the β-FeOOH nanoparticles as the coating substrates for PEG-PAsp in this study, exploring their potential utility in the MR imaging of solid tumors.

2. Experimental

2.1. Materials

β-Benzyl L-aspartate and bis(trichloromethyl)carbonate (triphosgene) were purchased from Sigma Chemical Co. Inc. (St. Louis, MO) and Tokyo Kasei Kogyo Co. Inc. (Tokyo, Japan), respectively. Iron(III) chloride hexahydrate ($FeCl_3 \cdot 6H_2O$) was purchased from Wako Pure Chemical Co. Inc. (Osaka, Japan). α-Methoxy-ω-amino-poly(ethylene glycol) (CH_3O-PEG-NH_2; $M_w = 12{,}000$) was purchased from Nippon Oil and Fats Co. Ltd. (Tokyo, Japan). Tetrahydrofuran (THF), *n*-hexane, *N,N*-dimethylformamide (DMF), CH_2Cl_2 were doubly distilled following standard procedures. Murine colon adenocarcinoma 26 (C-26) cells were kindly supplied by Dr. Y. Matsumura, the National Cancer Center Research Institute East, Japan (Kashiwa, Japan). C-26 cells were maintained in RPMI 1640 medium (Sigma Chemical) containing 10% fetal bovine serum in a humidified atmosphere with 5% CO_2 at 37 °C. CDF-1 mice (female, 6 weeks old) were purchased from Charles River, Japan. The animals were cared for and all experiments were performed in compliance with the Guide for the Care and Use of Laboratory Animals as adopted and promulgated by the National Institutes of Health.

2.2. Synthesis of poly(ethylene glycol)-poly(α,β-aspartic acid) block copolymer (PEG-PAsp)

PEG-PAsp was synthesized by a previously reported procedure [36] as follows: *N*-carboxy anhydride of β-benzyl L-aspartate (BLA-NCA) was synthesized by the Fuchs-Farthing method using triphosgene [37]. Poly(ethylene glycol)-poly(β-benzyl L-aspartate) block copolymer (PEG-PBLA) was synthesized by the polymerization of BLA-NCA in the mixed solvent of DMF and CH_2Cl_2 initiated from the terminal amino group of α-methoxy-ω-amino-poly(ethylene glycol) (CH_3O-PEG-NH_2; $M_w = 12{,}000$, M_w/M_n: 1.02). A narrow molecular weight distribution (M_w/M_n: 1.06) of PEG-PBLA was confirmed by gel permeation chromatography [columns: TSK-gel G3000HHR, G4000HHR (Tosoh, Yamaguchi, Japan); eluent: DMF containing 10 mM LiCl; flow rate: 0.8 ml/min; detector: refractive index (RI); temperature: 40 °C]. The structure and the composition of PEG-PBLA was analyzed by 270 MHz ^{1}H NMR [JEOL EX270 (Tokyo, Japan); solvent: DMSO-d_6; temperature: 80 °C]. The polymerization degree of BLA were determined to be 39 from the peak intensity ratio of the methylene protons of PEG (OCH_2CH_2: $\delta = 3.7$ ppm) and the phenyl protons of the β-benzyl groups of PBLA ($-CH_2C_6H_5$: $\delta = 7.3$ ppm). The deprotection of the benzyl group of PEG-PBLA was carried out under alkali condition (0.5N NaOH) at room temperature to obtain PEG-PAsp.

2.3. Preparation of iron oxide nanoparticles

A typical procedure yielding iron oxide nanoparticles is described as follows: 10 mM iron chloride $FeCl_3 \cdot 6H_2O$ aqueous solution was stirred at 4 °C for 1 h, and then incubated at 50 °C for 24 h. This solution was then quickly added into 2.5 wt% aqueous solution of PEG-PAsp. The final concentration of the polymer was adjusted to 0.5 wt%. The mixed solutions were incubated at room temperature for 24 h to obtain iron oxide nanoparticles coated with PEG-PAsp.

2.4. Physicochemical characterization of the nanoparticles

The morphology and the size distribution of nanoparticles were examined by energy filtering transmission electron microscopy (Carl Zeiss LEO922 EF-TEM) zero-loss images at an accelerating voltage of 160 kV. The TEM samples were prepared by mounting a drop of the aqueous suspension of the iron oxide nanoparticles on carbon-coated 400 mesh Cu grids and allowing them to dry in air. The X-ray diffraction spectrum of the nanoparticles is collected on a MAC Science M18XHF diffractometer, using a monochromatized X-ray beam with Cu Kα radiation ($\lambda = 1.54056$ Å, 40 kV, 200 mA, and $10° < 2\theta < 90°$). Fourier transform infrared (FT-IR) spectra were obtained using

a JASCO 615 FT-IR spectrophotometer with a resolution of 4 cm^{-1}. To characterize the coated layer of PEG-PAsp on the nanoparticles, a small amount of nanoparticles powder was milled with KBr, and was pressed into a disc for analysis. Each spectrum was scanned over 64 times to increase the signal-to-noise ratio. The Fe content in the micelles was determined by an ion coupled plasma-mass spectroscopy (ICP-MS, Hewlett Packard 4500).

2.5. Light scattering and ζ-potential measurements

The size distribution of the PEG-coated iron hydroxide nanoparticles was evaluated by a dynamic light scattering DLS-7000 (Otsuka Electronics, Osaka, Japan). Vertically polarized light with a wavelength of 488 nm from Ar-ion laser (15 mW) was used as the incident beam. All measurements were conducted at 25 °C, and data were analyzed by the cumulant method to determine the hydrodynamic diameters of the particles. The ζ-potential of the nanoparticles at 25 °C were determined by employing a Zetasizer NanoZS instrument equipped with a DTS5001 cell on a Malvern 4700 system.

2.6. Characterization of the R_1 and R_2 relaxivities

The MR contrast effect of the iron hydroxide nanoparticles was examined by measuring their proton relaxivities, R_1 and R_2. The iron hydroxide samples were dissolved into deionized water at concentrations of 0.5, 1.0, 1.5, 2.0, 2.5 mM and the relaxivity calculation of these nanoparticles solutions were performed at 25 °C in water with a 0.47 T minispectrometer (Minispec Bruker). The inversion recovery method and the Carr-Purcell-Meiboom-Gill (CPMG) method were used, respectively, for determining T_1 and T_2.

2.7. In vivo mouse MR imaging

CDF1 mice (female) were inoculated subcutaneously with C-26 cells (1×10^6). After 14 days, MR imaging of the tumor was conducted with a 4.7 T scanner (Varian INOVA200). The imaging was performed at the different temporal points (e.g., preinjection, 1 h postinjection, and 3 h postinjection) after the intravenous tail injection of the Feridex® and the PEG-PAsp-coated iron hydroxide nanoparticles (1 and 0.1 mmol/kg of Fe). For the T_2-weighted MR imaging of a live mouse, the following parameters were adopted: point resolution = 234 μm × 234 μm, section thickness = 2.0 mm, TE = 30 ms, TR = 3000 ms, number of acquisitions = 5. For the T_2 mapping of a live mouse, the following parameters were adopted: point resolution = 234 μm × 234 μm, section thickness = 2.0 mm, TE = 20, 40, 60, 80, and 100 ms, TR = 3000 ms, number of acquisitions = 5. The T_2 mappings were calculated from five spin-echo MR images by means of a linear least-squares curve fitting on a pixel-by-pixel basis with Mathematica®. Fitting of the signal intensity for the ith, jth pixel as a function of time, t, can be expressed as follows: $SI_{i,j}(t) = SI_{0i,j} \exp(-t/T_{2i,j})$, where $SI_{0i,j}$ is the pixel intensity at $t = 0$ and $T_{2i,j}$ is the T_2 time constant of pixel i, j. A magnitude image is generated from the pixel $SI_{0i,j}$ data, and a T_2 map is generated from the $T_{2i,j}$ data.

3. Results and discussion

Surface modification of iron oxide nanoparticles with biocompatible polymers such as PEG, is potentially beneficial to prepare MR contrast agents for *in vivo* applications. In particular, an anti-fouling or protein-resistant property is required for the nanoparticles to achieve the longevity in the blood circulation, accumulating in tumors by the enhanced permeability and retention (EPR) effect [38]. Otherwise, nanoparticles may be promptly captured by RES due to the opsonization through the non-specific interaction with the plasma components [17,18]. To provide the nanoparticles with non-fouling properties, we established an effective procedure of forming PEG-coated layer on the iron hydroxide nanoparticles through their simple soaking into the PEG-PAsp aqueous solution.

The parent nanoparticles were synthesized by stirring 10 mM iron chloride, $FeCl_3 \cdot 6H_2O$, aqueous solution at 4 °C for 1 h, followed by an incubation at 50 °C for 24 h. This reaction was carried out in water in the absence of organic stabilizers such as dextran. The TEM image in Fig. 1 shows that the prepared nanoparticles were substantially homogeneous both in the size and the shape. Most of the particles have a needle shape, approximately 60 nm length and 10 nm in width. There are a few crystalline grains with the shape of crosses or six-arm stars. Statistical analysis of the TEM micrograph revealed that the long axis and the short axis of the needle-shaped nanoparticles were 60 ± 12 nm and 10 ± 3 nm, respectively. The phase analysis was also performed by a X-ray powder diffraction. Fig. 2 shows the X-ray diffraction pattern of the powdered sample, which matched well with those of JCPDS card 34-1266 for the β-FeOOH (alkaganeite). The line broadening indicated that the samples were composed of the small particles of several nanometers in the size. Fig. 3 shows a plot of the iron oxide nanoparticles concentration versus R_1 and R_2. The relaxivities

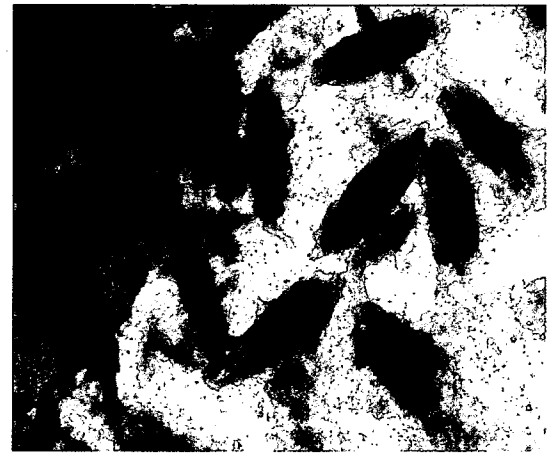

Fig. 1. EFTEM zero-loss image of β-FeOOH nanoparticles.

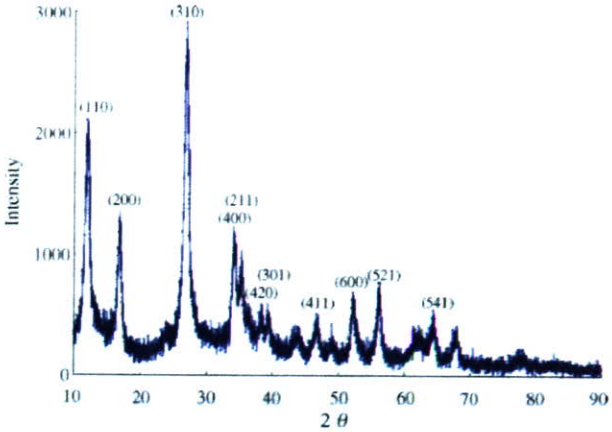

Fig. 2. X-ray powder diffraction patterns of the β-FeOOH nanoparticles.

of these β-FeOOH nanoparticles were indicated to be 4.00 and 4.80 $mM^{-1}\ s^{-1}$, which were significantly smaller than those for the dextran-coated iron oxide nanoparticles [16]. The low magnetic properties of the β-FeOOH nanoparticles may be a major cause for the smaller relaxivity values.

Transmission electron micrographs gave further insight into the structure of the PEG-PAsp-coated β-FeOOH nanoparticles. Energy filtering transmission electron microscopy was used to estimate the thickness of the polymer layer of the PEG-coated iron hydroxide nanoparticles. Fig. 4 shows the zero-loss images of the nanoparticle with 160 kV accelerating voltages. Note that in a normal TEM image non-elastic as well as elastic scattering electrons were detected, whereas elastic scattering electrons were only detected in the zero-loss image from the PEG layer and the iron oxide core. Therefore, we can recognize the PEG layer

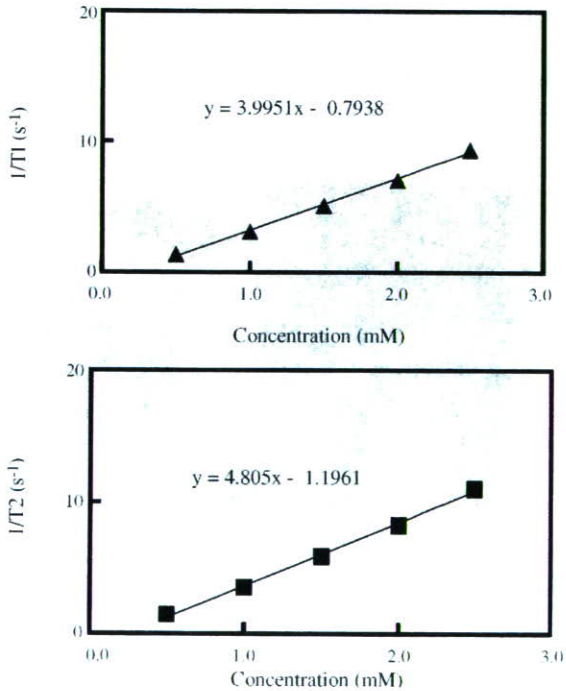

Fig. 3. Proton relaxivities, R_1 and R_2, of novel contrast agent at 0.47 T, 25 °C.

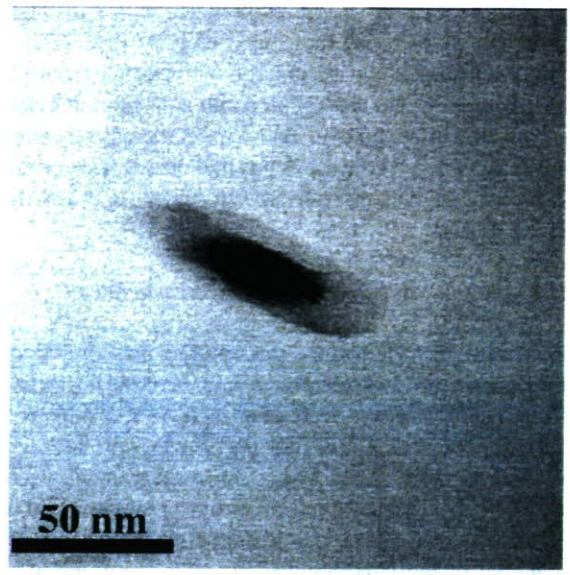

Fig. 4. EFTEM zero-loss image of the PEG-PAsp-coated β-FeOOH nanoparticles.

selectively on the PEG-coated iron oxide nanoparticles in the zero-loss image. Consequently, the thickness of the PEG layer on the iron oxide nanoparticles was estimated to be 10–15 nm. The long axis length of the PEG-coated nanoparticles determined from the zero-loss image was consistent with the cumulant diameter of the PEG-coated nanoparticles obtained by DLS (Fig. 5). The negligible discrepancy in the PEG thickness between the dry and the wet samples may presumably be due to the relatively high density of the PEG brushes on the iron oxide surface. Note that the end-to-end distances (R) of PEG [M = 5000 g/mol, degree of polymerization (DP) = 113] based on zigzag, meander, and random coil models were calculated to be 47.6, 24.5–27.2, and 5.9 nm, respectively [39]. Thus, it is likely that the PEG strands immobilized on the β-FeOOH nanoparticles may adopt a conformation of the slightly stretched random coil.

To confirm the PEG-PAsp coating of the β-FeOOH nanoparticles, the zeta potential was measured for the bare and the PEG-PAsp-coated β-FeOOH nanoparticles as a function of pH (Fig. 6). The iso-electric point (iep) of the bare β-FeOOH was determined as approximately 9, being consistent with the range of the reported iep value of iron oxide [40]. At the pH lower than the iep, the β-FeOOH nanoparticle surface should be

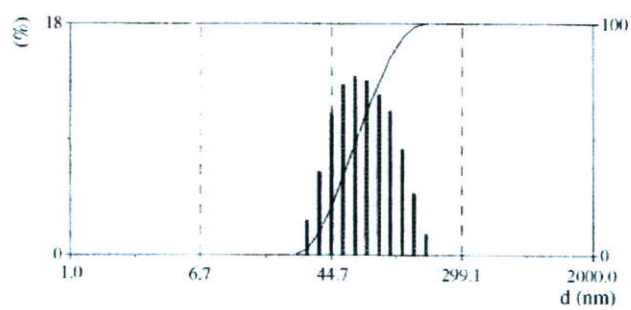

Fig. 5. DLS histogram of the PEG-PAsp-coated β-FeOOH nanoparticles at 25 °C.

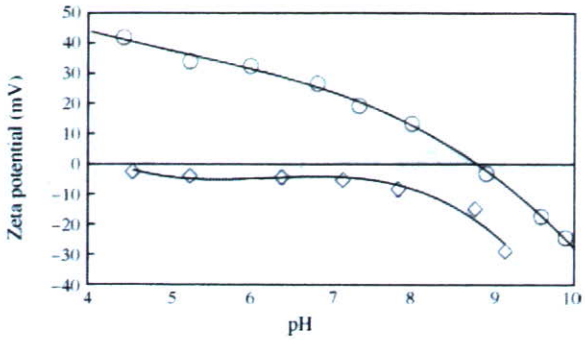

Fig. 6. Influence of pH on the zeta potential of bare β-FeOOH nanoparticles (○) and PEG-PAsp-coated β-FeOOH nanoparticles (◇).

protonated to give a positive zeta potential. Thus, in this region, an electrostatic attraction between the positively charged β-FeOOH nanoparticle and the negatively charged PEG-PAsp is expected to occur, allowing the PEG-PAsp adsorption to the nanoparticle surface. Indeed, the bare β-FeOOH nanoparticles possess a positive zeta potential at physiological pH, whereas the zeta potential shifted to the neutral value for the PEG-PAsp-modified nanoparticles. This data supports the adsorption mechanism that the carboxylic acid moieties of PAsp segments of the block copolymer electrostatically bound to the iron oxide particle surface, formulating a PEG outer layer.

To get a further insight into the mechanism of the PEG-PAsp interaction with the β-FeOOH, the infrared spectra of the PEG-PAsp adsorbed on the β-FeOOH particles were examined. Infrared spectra of PEG-PAsp sodium salt and the PEG-PAsp adsorbed onto the iron oxide particles are compared in Fig. 7. The main peaks and their positions are summarized in Table 1.

Two major anchoring mechanisms of a carboxylate compound to a metal surface, hydrogen bonding and coordination bonding (complexation), can be separately identified in a vibrational spectroscopy. Hamilton and Ibers [41] found that the involvement of hydrogen bonding substantially change the O–H stretching frequency or bandwidth: strong hydrogen bonding

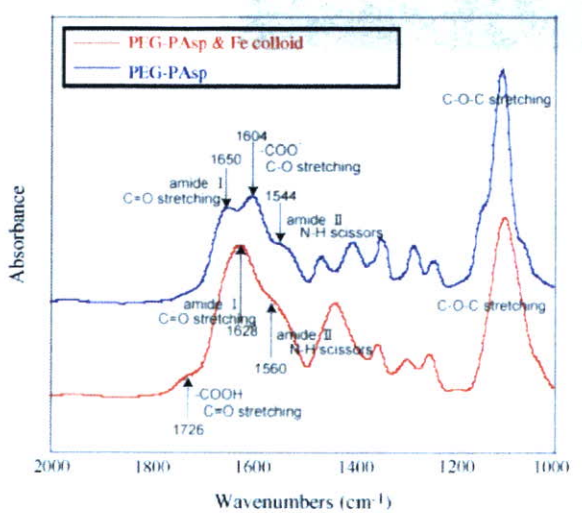

Fig. 7. FT-IR spectra of PEG-PAsp sodium salt and PEG-PAsp adsorbed onto β-FeOOH nanoparticles.

Table 1
The major infrared vibration modes summarized for PEG-PAsp sodium salt and PEG-PAsp adsorbed onto β-FeOOH particles

Peak positions (cm^{-1})[a]		Peak assignment
Free polymer	Polymer on β-FeOOH	
	1717sh	ν(C=O) free carboxylic acid stretch
1650		ν(C=O) amide **I** (carbonyl stretch)
1604	1628	ν_{as}(C=O) antisymmetric carboxylate stretch
1544sh	1560sh	δ(N–H) + ν(C–N) amide **II** (NH bend and CN stretch)
1468		$\delta(CH_2)$ methylene scissors deformation
1406	1435	ν_s(C=O) symmetric carboxylate stretch
198	193	Δν (difference between ν_{as}(C=O) and ν_s(C=O))

[a] sh: shoulder.

causes a downward frequency shift while longer/weaker bonding has only a marginal effect [42]. If complexation involves, the characteristic frequencies of the carboxylate group in the polymer are expected to shift significantly.

Several studies have demonstrated that carboxylic acids and their salts adsorb as carboxylates on inorganic (oxide) surfaces [43–45], inducing the expected frequency shifts. When the carboxylate group is directly involved in the adsorption, it is able to discriminate those structures as the monodentate (**I**), the bidentate chelating (**II**), and the bidentate bridging (**III**) (Fig. 8) in the vibrational spectrum on the basis of the carboxylate asymmetric and symmetric stretches. The monodentate structure (**I**) has (formally) the distinct double (C=O) and single (C–O) bonds while the bidentate structures (**II** and **III**) have the two equivalent C–O bonds. The lower frequency (or the wave number) band of the bidentate structures (**II** and **III**) is assigned as the *sym* (COO–) stretching and the higher frequency band as the *asym* (COO–) stretching. In the case of the monodentate structure (**I**), the lower frequency band of the *sym* (COO–) reflects the more C–O character to induce even a lower shift in the frequency, while the higher frequency band of the *asym* (COO–) has the more C=O character to cause a further increase in the frequency. Eventually, for the monodentate structure, the *asym* (COO–) is observed at the considerably higher frequency region as ca. 1650 cm^{-1} and is indicative of the significant C=O character. In an opposite way, the absence of the *asym* stretching band in this region should be one of the good indicates for the formation of the bidentate structures. Also, the frequential or the wave number difference of the *sym* and the *asym* bands ($\Delta\nu = \nu_{asym} - \nu_{sym}$) can be a measure to

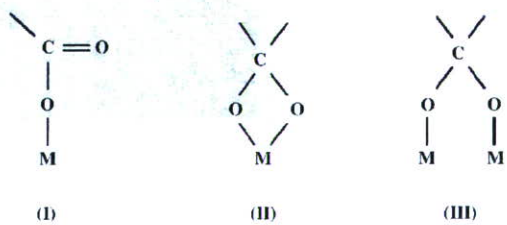

Fig. 8. Modes of carboxylate-metal complexation: monodentate (**I**), bidentate chelating (**II**), and bidentate bridging (**III**).

discriminate the bidentate and the monodentate structures, using a standard carboxylate salt as a control [46]:

- *Monodentate* (**I**). Characteristic C=O band is observed in the spectrum with $\Delta\nu$ being greater than the standard $\Delta\nu$ for the carboxylate salt.
- *Bidentate chelating* (**II**). No characteristic C=O band is observed in the spectrum with $\Delta\nu$ being smaller than the standard $\Delta\nu$ for the carboxylate salt.
- *Bidentate bridging* (**III**). No characteristic C=O band is observed in the spectrum with $\Delta\nu$ being equivalent to $\Delta\nu$ for the carboxylate salt.

In the case of the PEG-PAsp adsorption to the β-FeOOH surface, $\Delta\nu_{(ads)}$ is evaluated to be smaller or similar to $\Delta\nu_{(free)}$ ($\Delta\nu_{(ads)} \sim 193$, $\Delta\nu_{(free)} \sim 198$), suggesting the bidentate chelation to be the major mode of this anchoring process. Although there is a weak band at ca. 1717 cm^{-1} possibly assigned to C=O stretching, there is still no indication of the corresponding C–O band at 1382 cm^{-1} in the spectrum. There is also no evidence for the hydrogen-bonded C=O group in these spectra. This is in the agreement with the observation by Kirwan et al. [47] that shows the polyacrylate adsorption onto hematite at low pH to occur via the bidentate chelation mechanism. The OH stretches at 3500 cm^{-1} are not resolved, as the β-FeOOH surface has not been dehydrated, and it was not able to discriminate these possible modes of hydrogen bonding. Consequently, the PEG-PAsp bound to the nanoparticle surface via the PAsp segment by both bidentate chelation and electrostatic interaction to form the tethering PEG layer as a palisade.

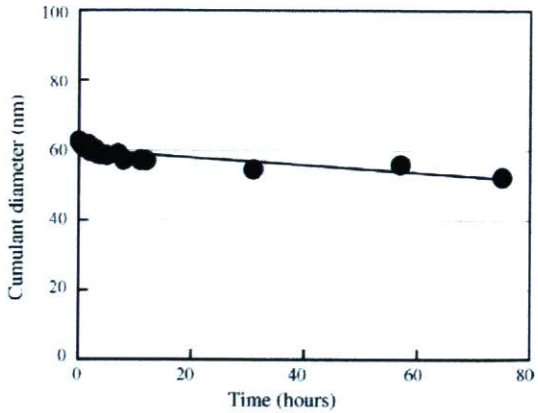

Fig. 9. Hydrodynamic diameters as a function of storage time at 37 °C the PEG-PAsp-coated β-FeOOH nanoparticles in 0.15 M sodium chloride solution.

The stability in biological media is critical for an MRI contrast agent because it directly correlates with the *in vivo* performance. Also, the storage stability of the nanoparticles is an important factor from a practical standpoint. It should be stressed that electrostatically stabilized nanoparticles are stable in the aqueous solution without salt, but are likely to undergo a fast aggregation by the salt addition due to the reduction in an electrical repulsive force. Only a few examples are known

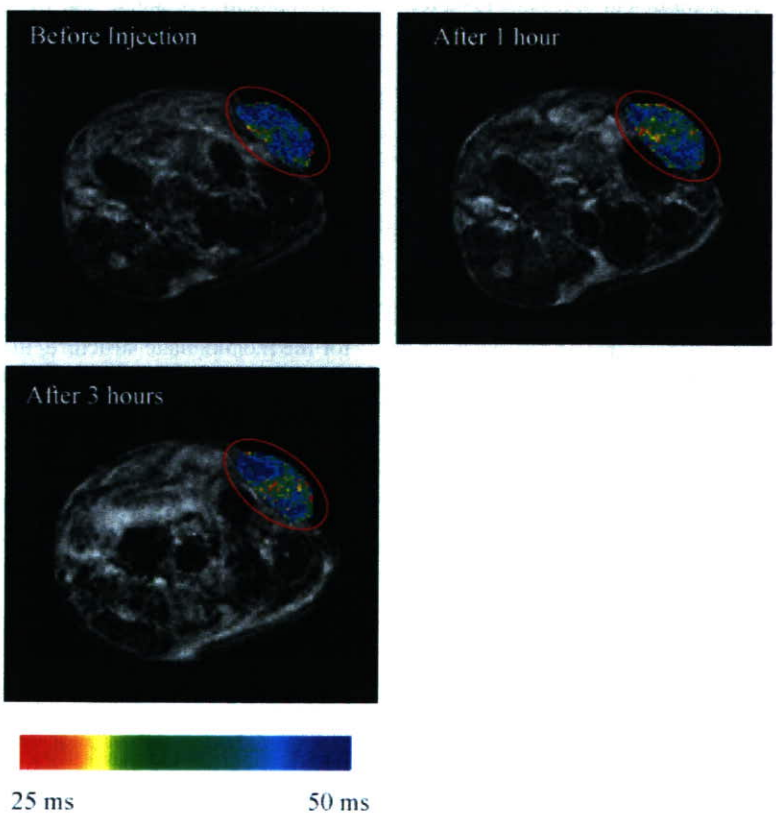

Fig. 10. T_2-weighted images of tumor-implanted mouse at 4.7 T and T_2 color maps (tumor site in red circle) at different temporal points after the PEG-PAsp-coated β-FeOOH nanoparticles injection.

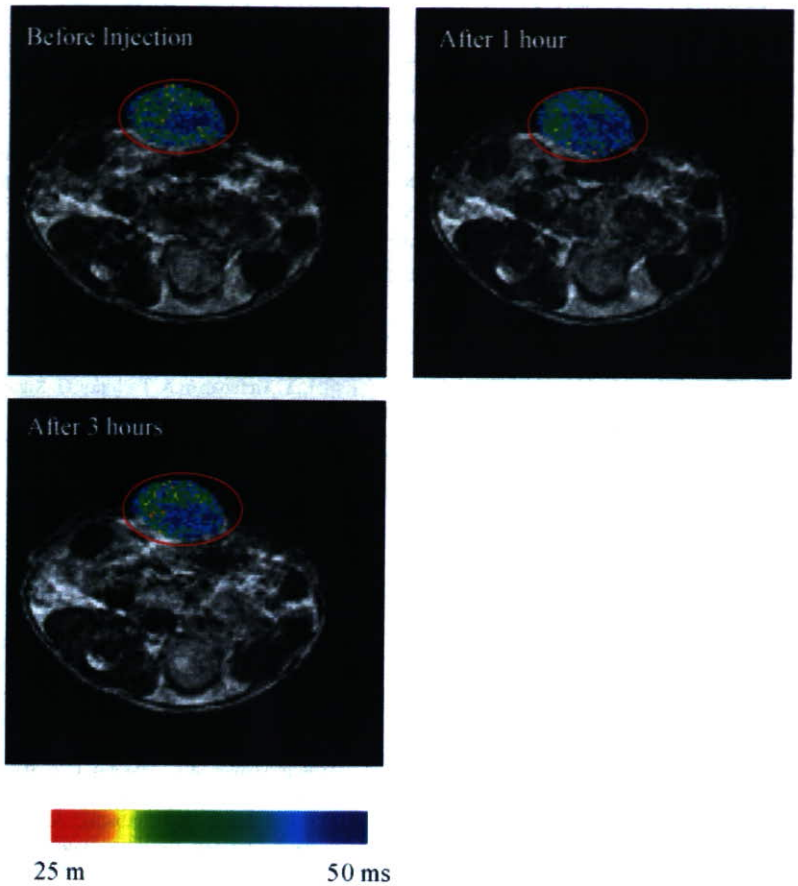

Fig. 11. T_2-weighted images of tumor-implanted mouse at 4.7 T and T_2 color maps (tumor site in red circle) at different temporal points after Feridex® injection.

where a long-term stability is reported at the salt concentration as high as in the physiological level. To evaluate the colloidal stability of the PEG-PAsp-coated nanoparticles prepared here, they were incubated in 0.15 M sodium chloride solution at 37 °C with measuring the hydrodynamic diameters at a definite time interval (Fig. 9). Obviously, almost no change in the particle size is detectable during the 80 h of the storage time. The particles were further stored for a month in 0.15 M sodium chloride solution to show no change in their size (data not shown). These results indicate the high stability of these PEG-PAsp-coated nanoparticles in physiological conditions.

We then examined an applicability of the PEG-PAsp-coated nanoparticles for the *in vivo* tumor imaging based on a T_2 mapping, which is a useful way to evaluate the tumor accumulation of the contrast agent quantitatively in a spatial manner because T_2 of every voxels can be determined separately through the T_2 mapping method. Tumor-bearing mice were prepared by the subcutaneous injection of the C-26 cell line into the abdominal part of the mice. MR imaging of the mice was performed at the scheduled time points after the intravenous injection of Feridex® and the PEG-PAsp-coated β-FeOOH nanoparticles solution (1 and 0.1 mmol/kg of Fe, respectively). Color mapping of the identical MR images shows more details of the MR signal changes (Figs. 10 and 11). The T_2 was calculated as described in Section 2. Green, yellow, and red regions corresponds to the low T_2 value, while blue region corresponds to the high T_2 value. In the control experiment with Feridex® (1 mmol/kg of Fe), no change in the color-mapped MR signal and the T_2 values at the tumor site (red circled region in Fig. 11) was observed. In contrast, at 1 h postinjection of the PEG-coated β-FeOOH nanoparticles (the red circled region in Fig. 10), green, yellow, and red regions increased the occupation of roughly 1/2 of the tumor tissues, indicative of the accumulation of the detectable amounts of the PEG-PAsp-coated β-FeOOH nanoparticles within the tumor. At 3 h postinjection, green, yellow, and red regions slightly decreased the occupation of roughly 1/3 of the tumor tissues relative to that of the control. This suggests that the tumor imaging is feasible for up to 3 h with the i.v. injected PEG-PAsp-coated β-FeOOH nanoparticles. The higher accumulation of the PEG-PAsp-coated β-FeOOH nanoparticles within the tumor as compared to that of Feridex® may be attributed to their smaller size and the neutral surface charge, resulting in the higher feasibility of the penetration into the tumor.

4. Conclusion

In conclusion, we reported here a simple route to synthesize PEG-coated iron oxide nanoparticles by hydrolysis of $FeCl_3 \cdot 6H_2O$ in water and the subsequent treatment with the PEG-PAsp block copolymers. The FT-IR experimental results proved that PEG-PAsp molecules are multi-valently bound to

the surface of the iron oxide nanoparticles via the coordination between the carboxylic acids in the PAsp segment of the block copolymer and Fe on the surface of the iron hydroxide nanoparticles. Hence the resultant nanoparticles possess an excellent solubility and a stability in aqueous solution as well as in physiological saline. *In vivo* MRI experimental results also indicated that the iron hydroxide nanoparticles prepared by the current approach possess the accumulation property into tumor, which suggests their potential utility as tumor-targeting MRI contrast agents.

Acknowledgements

This work was supported by a Grant-in-Aid for Scientific Research from the Ministry of Education, Culture, Sports, Science and Technology (MEXT), Core Research for Evolution of Science and Technology (CREST), Japan Science and Technology Corporation (JST), and 21st century COE program 'Human-Friendly Materials based on Chemistry' from MEXT.

References

[1] M. Baghi, M.G. Mack, M. Hambek, J. Rieger, T. Vogl, W. Gstoettner, R. Knecht, Anticancer Res. 25 (2005) 3665–3670.
[2] M.S. Martina, J.P. Fortin, C. Ménager, O. Clément, G. Barratt, C. Grabielle-Madelmont, F. Gazeau, V. Cabuil, S. Lesieur, J. Am. Chem. Soc. 127 (2005) 10676–10685.
[3] R.G. Blasberg, Mol. Cancer Ther. 2 (2003) 335–343.
[4] D. Artemov, J. Cell. Biochem. 90 (2003) 518–524.
[5] S.A. Schmitz, RoFo Fortschr. Geb. Roentgenstr. Nuklearmed. 175 (2003) 469–476.
[6] L.J. Kroft, A. de Roos, J. Magn. Reson. Imaging 10 (1999) 395–403.
[7] B. Bonnemain, J. Drug Targeting 6 (1998) 167–174.
[8] M.F. Bellin, C. Beigelman, S. Precetti-Morel, Eur. J. Radiol. 34 (2000) 257–264.
[9] N. Kohler, C. Sun, J. Wang, M. Zhang, Langmuir 21 (2005) 8858–8864.
[10] A.K. Gupta, A.S. Curtis, J. Mater. Sci.: Mater. Med. 15 (2004) 493–496.
[11] H. Lee, E. Lee, D.K. Kim, N.K. Jang, Y.Y. Jeong, S. Jon, J. Am. Chem. Soc. 128 (2006) 7383–7389.
[12] Y.M. Huh, Y.W. Jun, H.T. Song, S. Kim, J.S. Choi, J.H. Lee, S. Yoon, K.S. Kim, J.S. Shin, J.S. Suh, J.W. Cheon, J. Am. Chem. Soc. 127 (2005) 12387–12391.
[13] A.K. Gupta, M. Gupta, Biomaterials 26 (2005) 3995–4021.
[14] A. Ito, Y. Kuga, H. Honda, H. Kikkawa, A. Horiuchi, Y. Watanabe, T. Kobayashi, Cancer Lett. 212 (2004) 167–175.
[15] C. Grüttner, J. Teller, W. Schütt, Scientific and Clinical Applications of Magnetic Carriers, Plenum Press, New York, 1997, p. 53.
[16] Y.J. Wang, S.M. Hussain, G.P. Krestin, Eur. Radiol. 11 (2001) 2319–2331.
[17] I. Raynal, P. Prigent, S. Peyramaure, A. Najid, C. Rebuzzi, C. Corot, Invest. Radiol. 39 (2004) 56–63.
[18] W.J. Rogers, P. Basu, Atherosclerosis 178 (2005) 67–73.
[19] D.B. Shieh, F.Y. Cheng, C.H. Su, C.S. Yeh, M.T. Wu, Y.N. Wu, C.Y. Tsai, C.L. Wu, D.H. Chen, C.H. Chou, Biomaterials 26 (2005) 7183–7191.
[20] N. Kohler, G.E. Fryxell, M. Zhang, J. Am. Chem. Soc. 126 (2004) 7206–7211.
[21] M. Mikhaylova, D.K. Kim, N. Bobrysheva, M. Osmolowsky, V. Semenov, T. Tsakalakos, M. Muhammed, Langmuir 20 (2004) 2472–2477.
[22] C.L. Kaufman, M. Williams, L.M. Ryle, T.L. Smith, M. Tanner, C. Ho, Transplantation 76 (2003) 1043–1046.
[23] C.C. Berry, S. Wells, S. Charles, G. Aitchison, A.S. Curtis, Biomaterials 25 (2004) 5405–5413.
[24] Y. Zhang, N. Kohler, M. Zhang, Biomaterials 23 (2002) 1553–1561.
[25] A.J. D'Souza, R.L. Schowen, E.M. Topp, J. Contr. Release 94 (2004) 91–100.
[26] L.X. Tiefenauer, A. Tschirky, G. Kühne, R.Y. Andres, Magn. Reson. Imaging 14 (1996) 391–402.
[27] S.M. Moghimi, A.C. Hunter, J.C. Murray, Pharmacol. Rev. 53 (2001) 283–318.
[28] A.F. Thünemann, D. Schütt, L. Kaufner, U. Pison, H. Möhwald, Langmuir 22 (2006) 2351–2357.
[29] J.F. Lutz, S. Stiller, A. Hoth, L. Kaufner, U. Pison, R. Cartier, Biomacromolecules 7 (2006) 3132–3138.
[30] D.D. Stark, R. Weissleder, G. Elizondo, P.F. Hahn, S. Saini, L.E. Todd, J. Wittenberg, J.T. Ferrucci, Radiology 168 (1988) 297–301.
[31] R. Weissleder, G. Elizondo, J. Wittenberg, C.A. Rabito, H.H. Bengele, L. Josephson, Radiology 175 (1990) 489–493.
[32] C.W. Jung, P. Jacobs, Magn. Reson. Imaging 13 (1995) 661–674.
[33] R. Weissleder, A. Bogdanov, E.A. Neuwelt, M. Papisov, Adv. Drug Deliv. Rev. 16 (1995) 321–334.
[34] K.E. Garcia, A.L. Morales, C.A. Barrero, C.E. Arroyave, J.M. Greneche, Phys. B: Condens. Matter 354 (2004) 187–190.
[35] F.J. Lázaro, A.R. Abadia, M.S. Romero, L. Gutiérrez, J. Lázaro, M.P. Morales, Biochim. Biophys. Acta: Mol. Basis Dis. 1740 (2005) 434–445.
[36] N. Nishiyama, M. Yokoyama, T. Aoyagi, T. Okano, Y. Sakurai, K. Kataoka, Langmuir 15 (1999) 377–383.
[37] W.H. Daly, D. Poché, Tetrahedron Lett. 29 (1988) 5859–5862.
[38] Y. Matsumura, H. Maeda, Cancer Res. 46 (1986) 6387–6392.
[39] S. Takae, Y. Akiyama, H. Otsuka, T. Nakamura, Y. Nagasaki, K. Kataoka, Biomacromolecules 6 (2005) 818–824.
[40] L. Cromières, V. Moulin, B. Fourest, E. Giffaut, Colloids Surf. A 202 (2002) 101–115.
[41] W.C. Hamilton, J.A. Ibers, Hydrogen Bonding in Solids: Methods of Molecular Structure Determination, Benjamin, New York, 1968.
[42] H. Ratajczak, W.J. Orville-Thomas, J. Mol. Struct. 1 (1968) 449–461.
[43] F. Bournel, C. Laffon, P. Parent, G. Tourillon, Surf. Sci. 352–354 (1996) 228–231.
[44] K. Ishiduki, K. Esumi, J. Colloid Interf. Sci. 185 (1997) 274–277.
[45] E. Papirer, J.-M. Perrin, G. Nanse, P. Fioux, Eur. Polym. J. 30 (1994) 985–991.
[46] K. Nakamoto, Infrared and Raman Spectra of Inorganic and Coordination Compounds, John Wiley & Sons, New York, 1986.
[47] L.J. Kirwan, P.D. Fawell, W. van Bronswijk, Langmuir 19 (2003) 5802–5807.

Improvement of cancer-targeting therapy, using nanocarriers for intractable solid tumors by inhibition of TGF-β signaling

Mitsunobu R. Kano*†‡, Younsoo Bae‡§, Caname Iwata*¶, Yasuyuki Morishita*, Masakazu Yashiro‖, Masako Oka*, Tomoko Fujii*, Akiyoshi Komuro*, Kunihiko Kiyono*, Michio Kaminishi¶, Kosei Hirakawa‖, Yasuyoshi Ouchi†, Nobuhiro Nishiyama§**, Kazunori Kataoka‡§**††, and Kohei Miyazono*‡‡

Departments of *Molecular Pathology, †Geriatrics, ¶Gastrointestinal Surgery, and §Center for Disease Biology and Integrative Medicine, Graduate School of Medicine; **Department of Materials Engineering, Graduate School of Engineering; and ‡Center for Nano-Bio Integration, University of Tokyo, Tokyo 113-0033 Japan; and ‖Department of Surgical Oncology, Osaka City University Graduate School of Medicine, Osaka 545-8585, Japan

Communicated by Tadatsugu Taniguchi, University of Tokyo, Tokyo, Japan, December 28, 2006 (received for review December 25, 2006)

Transforming growth factor (TGF)-β plays a pivotal role in regulation of progression of cancer through effects on tumor microenvironment as well as on cancer cells. TGF-β inhibitors have recently been shown to prevent the growth and metastasis of certain cancers. However, there may be adverse effects caused by TGF-β signaling inhibition, including the induction of cancers by the repression of TGF-β-mediated growth inhibition. Here, we present an application of a short-acting, small-molecule TGF-β type I receptor (TβR-I) inhibitor at a low dose in treating several experimental intractable solid tumors, including pancreatic adenocarcinoma and diffuse-type gastric cancer, characterized by hypovascularity and thick fibrosis in tumor microenvironments. Low-dose TβR-I inhibitor altered neither TGF-β signaling in cancer cells nor the amount of fibrotic components. However, it decreased pericyte coverage of the endothelium without reducing endothelial area specifically in tumor neovasculature and promoted accumulation of macromolecules, including anticancer nanocarriers, in the tumors. Compared with the absence of TβR-I inhibitor, anticancer nanocarriers exhibited potent growth-inhibitory effects on these cancers in the presence of TβR-I inhibitor. The use of TβR-I inhibitor combined with nanocarriers may thus be of significant clinical and practical importance in treating intractable solid cancers.

angiogenesis | gastric cancer | molecular targeting therapy | pancreatic cancer

Chemotherapy that uses nanocarriers has been developed to improve the clinical treatment of solid tumors by obtaining high accumulation of drugs in tumor tissues but limited accumulation in normal organs. Doxil (1), a liposomal adriamycin (ADR), is one such drug that has already been used clinically (2). Doxil has exhibited therapeutic effects on some cancers with hypervascular characteristics (3, 4), including Kaposi sarcoma and ovarian cancers. Another promising formulation of nanocarriers is polymeric micelles (5, 6), which are already being used in clinical trials (7, 8).

However, despite the urgent need for effective chemotherapy for intractable solid tumors, including pancreatic adenocarcinoma (9) and diffuse-type gastric carcinoma (10), nanocarriers of any design have not been successful yet in exhibiting significant therapeutic effects on these cancers. Pancreatic cancer is the fourth leading cause of cancer-related death in the United States and the fifth in Japan (9), and the median survival period of patients who suffer from advanced pancreatic adenocarcinoma is still extremely short (≈6 months), despite recent progress in development of conventional chemotherapies (11). Although cancer cells derived from these tumors are sufficiently sensitive *in vitro* to conventional anticancer agents such as ADR (12), most of these agents have failed to exhibit sufficient therapeutic effects *in vivo*, regardless of formulation, whether encapsulated in nanocarriers or not. The theoretical basis of the specific accumulation of nanocarriers in tumor tissues is leakiness of tumor vessels to the macromolecular agents, termed the "enhanced permeability and retention (EPR) effect," which was demonstrated and named by Maeda *et al.* (13, 14). The major obstacles to treatment of these cancer cells could thus be insufficient EPR effect because of certain characteristics of their cancer microenvironment, including hypovascularity and thick fibrosis (15, 16). However, methods of regulating this effect have not been well investigated.

Transforming growth factor (TGF)-β signaling plays a pivotal role in both the regulation of the growth and differentiation of tumor cells and the functional regulation of tumor interstitium (17). Because TGF-β is a multifunctional cytokine that inhibits the growth of epithelial cells and endothelial cells and induces deposition of extracellular matrix, inhibition of TGF-β signaling in cancer cells and fibrotic components has been expected to facilitate the effects of anticancer therapy. TGF-β binds to type II (TβR-II) and type I receptors (TβR-I), the latter phosphorylates Smad2 and −3. Smad2 and −3 then form complexes with Smad4, translocate into the nucleus, and regulate the transcription of target genes (18). Several small-molecule TβR-I inhibitors have been reported to prevent metastasis of some cancers (19). However, there may be adverse effects of TGF-β inhibition, including potential progression of some cancers because of the repression of TGF-β-mediated growth inhibition of epithelial cells (20).

In this study, we show that administration of the small-molecule TβR-I inhibitor (LY364947) (21) at a low dose, which could minimize the potential side effects of TβR-I inhibitor, can alter the tumor microenvironment and enhance the EPR effect. This effect of low-dose TβR-I inhibitor was demonstrated with two of nanocarriers, i.e., Doxil and a polymeric micelle incorporating ADR (micelle ADR) that we have recently developed (22) [supporting information (SI) Fig. 7]. The present findings strongly suggest that our method, which uses a combination of

Author contributions: M.R.K., K. Kataoka, and K.M. designed research; M.R.K., Y.B., C.I., Y.M., M.O., T.F., A.K., and K. Kiyono performed research; M.Y. and K.H. contributed new reagents/analytic tools; M.R.K., Y.B., C.I., M.K., Y.O., N.N., K. Kataoka, and K.M. analyzed data; and M.R.K., N.N, K. Kataoka, and K.M. wrote the paper.

The authors declare no conflict of interest.

Freely available online through the PNAS open access option.

Abbreviations: ADR, adriamycin; EPR, enhanced permeability and retention; PECAM, platelet/endothelial cell adhesion molecule; TβR-I, type I transforming growth factor β receptor.

††To whom correspondence may be addressed at: Department of Material Engineering, Graduate School of Engineering, University of Tokyo, Tokyo 113-8656, Japan. E-mail: kataoka@bmw.t.u-tokyo.ac.jp.

‡‡To whom correspondence may be addressed. E-mail: miyazono-ind@umin.ac.jp.

This article contains supporting information online at www.pnas.org/cgi/content/full/0611660104/DC1.

www.pnas.org/cgi/doi/10.1073/pnas.0611660104

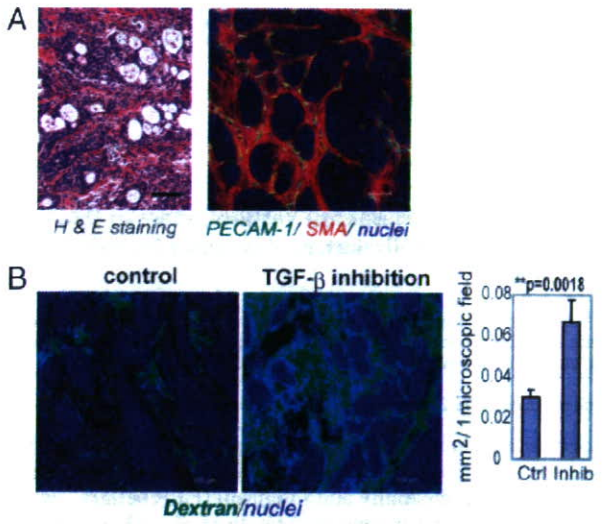

Fig. 1. Histology of BxPC3 xenograft and effects of low-dose TβR-I inhibitor. (*A*) The histology of the TGF-β-nonresponsive BxPC3 xenograft, used as a model of poorly differentiated pancreatic adenocarcinoma, shown in H&E staining and immunohistochemistry. Examination revealed nests of tumor cells in gland-like structures, with areas rich in fibrotic components (filled by α-smooth muscle actin (SMA)-positive myofibroblasts, shown in red) between them. The tumor tissue also includes some PECAM-1-positive vessels (shown in green) in the interstitium, although almost no vasculature was observed inside the nests of tumor cells. (*B*) Dextran leakage. At 24 h after administration of low-dose TβR-I inhibitor (1 mg/kg i.p.), i.v.-administered dextran of 2 MDa (50 nm in hydrodynamic diameter) exhibited broader distribution with 1 mg/kg TβR-I inhibitor (*Right*) than in the control (*Left*), which was quantified and shown in the graph ($n = 12$). Error bars in the graphs represent standard errors, and *P* values were calculated by Student's *t* test. Ctrl, control; Inhib, inhibitor. (Scale bars, 100 μm.)

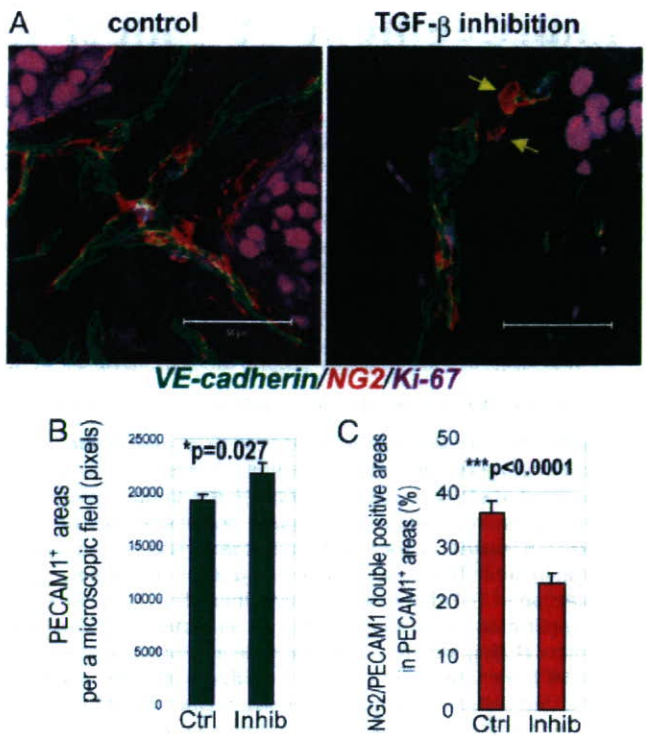

Fig. 2. Morphological changes in cancer neovasculature at 24 h after administration of low-dose TβR-I inhibitor. (*A*) Immunostaining of the tumor neovasculature. NG2-positive pericytes (shown in red) were dissociated (yellow arrows in *Right*) from VE-cadherin-positive endothelium (shown in green) after TβR-I inhibitor treatment for 24 h. (Scale bars, 50 μm.) (*B* and *C*) Areas of PECAM-1-positive endothelium (*B*) and pericyte-coverage (*C*) were quantified ($n = 40$) and are shown in the graphs. Error bars in the graphs represent standard errors, and *P* values were calculated by Student's *t* test. Ctrl, control; Inhib, inhibitor.

low-dose small molecule TβR-I inhibitor and long-circulating nanocarriers, is a promising way to treat intractable cancers.

Results

We used the xenografted BxPC3 human pancreatic adenocarcinoma cell line in nude mice as a disease model (Fig. 1). BxPC3 cells do not respond to TGF-β, because of lack of functional Smad4. Hematoxylin/eosin (H&E) staining of tumor tissue in this model (Fig. 1*A Left*) revealed poorly differentiated histology, with a certain number of blood vessels and thick fibrotic tissue in the interstitium. There was, however, almost no vasculature inside of tumor cell nests (Fig. 1*A Right*). This model thus represents the histological characteristics of some intractable solid tumors.

Systemic administration of low-dose TβR-I inhibitor in this model significantly altered the characteristic of tumor vasculature at 24 h after administration. We investigated the functional aspects of the effects of low-dose TβR-I inhibitor, using i.v.-administered large-molecule dextran of 2 MDa with a hydrodynamic diameter of 50 nm (23, 24), which is equivalent to the common sizes of nanocarriers (Fig. 1*B*). Although dextran of this molecular size for the most part remained in the intravascular space in the control condition, as reported in ref. 24, the use of TβR-I inhibitor resulted in a far broader distribution of this macromolecule around the tumor neovasculature. These findings suggest that low-dose TβR-I inhibitor can maintain blood flow in the tumor vasculature and simultaneously induce extravasation of macromolecules.

To investigate the mechanisms of effect of TβR-I inhibitor on the neovasculature, we analyzed the changes in three major components of tumor vasculature, i.e., endothelium, pericytes (Fig. 2), and basement membrane (SI Fig. 8), at 24 h after administration of TβR-I inhibitor. The areas of vascular endothelial cells stained by platelet/endothelial cell adhesion molecule (PECAM)-1 increased slightly with TβR-I inhibitor treatment (Fig. 2*B*). Although pericyte-coverage of endothelium has been reported to be incomplete in tumors (25), coverage of the endothelium by pericytes, which were determined as NG2-positive perivascular cells, was further decreased by the TβR-I inhibitor treatment. This finding was confirmed by comparing the ratios of PECAM-1/NG2-double-positive areas to PECAM-1-positive areas (Fig. 2*C*). On the other hand, vascular basement membrane, which was determined by staining with collagen IV, did not differ significantly in the presence or absence of TβR-I inhibitor (SI Fig. 8). We also examined the vasculature in normal organs and found that it was not affected by TβR-I inhibitor in terms of permeability of 2-MDa dextran and morphology on immunostaining (SI Fig. 9).

We next examined the effects of i.p. administration of small-molecule TβR-I inhibitor at a low dose (1 mg/kg) on TGF-β signaling, by determining phosphorylation of Smad2 (SI Figs. 10 and 11). Because it is a small-molecule agent, TβR-I inhibitor transiently suppressed phosphorylation of Smad2. In nucleated blood cells, phosphorylation of Smad2 was significantly suppressed at 1 h after administration of TβR-I inhibitor, but it gradually recovered toward 24 h. In contrast, phosphorylation of Smad2 in tumor cells and most interstitial cells was not suppressed even 1 h after administration, whereas a higher dose (25 mg/kg) of TβR-I inhibitor inhibited Smad2 phosphorylation in most tumor cells. Accordingly, the extent of fibrosis in cancer xenografts treated with low-dose TβR-I inhibitor did not differ